Addis Ababa University

Addis Ababa Institute of Technology

Electrical and Computer Engineering Department

Brain Tumor Detection and Segmentation Using Hybrid Intelligent Algorithms: Design and Implementation

By

Yehualashet Megersa

Advisor

Dr.Eng. Getachew Alemu

A Thesis Submitted to the School of Graduate Studies of Addis Ababa University in Partial Fulfillment of the Requirements for the Degree of Masters of Science in Electrical and Computer Engineering (Computer Engineering Stream)

November, 2012

Addis Ababa University

Addis Ababa Institute of Technology

Electrical and Computer Engineering Department

Brain Tumor Detection and Segmentation Using Hybrid Intelligent Algorithms: Design and Implementation

By

Yehualashet Megersa

Approval by Board of Examiners

Dr.-Ing. Dereje H/Mariam	_____
Chairman, Dept. Graduate Committee	Signature
Dr.Eng. Getachew Alemu	_____
Advisor	Signature
Dr. Eneyew Adugna	_____
Internal Examiner	Signature
Ato. Bisrat Derebssa	_____
External Examiner	Signature

Declaration

I, the undersigned, declare that this thesis is my original work, has not been presented for a degree in this or any other university, and all sources of materials used for the thesis have been fully acknowledged.

Yehualashet Megersa _____

Name Signature

Place: Addis Ababa

Date of Submission: November 16, 2012

This thesis has been submitted for examination with my approval as a university advisor.

Dr. Eng. Getachew Alemu _____

Advisor's Name Signature

Dedicated to My Parents

Abstract

In brain tumor diagnosis, clinicians integrate their medical knowledge and brain magnetic resonance imaging (MRI) scans to obtain the nature and pathological characteristics of brain tumors and to decide on treatment options. However, manually detecting and segmenting brain tumors in today's brain MRI, where a large number of MRI scans taken for each patient, is tedious and subjected to inter and intra observer detection and segmentation variability.

Therefore, there is a need for computer aided brain tumor detection and segmentation from brain MR images to overcome the tedium and observer variability involved in the manual segmentation. As result a number of methods have been proposed in recent years to fill this gap, but still there is no commonly accepted automated technique by clinicians to be used in clinical floor due to accuracy and robustness issues.

In this thesis, an automatic brain tumor detection and segmentation framework that consists of techniques from skull stripping to detection and segmentation of brain tumors is proposed with fuzzy Hopfield neural network as its final tumor segmentation technique. Through preprocessing, image fusion and initial tumorous slice classification, the final hybrid intelligent fuzzy Hopfield neural network algorithm based tumor segmentation, and tumor region detection and extraction is achieved.

The performance of the proposed framework is evaluated on various MR images including simulated and real, normal and tumorous. Quantitatively the method is validated against available ground truth (manual detection and segmentation) using commonly used validation metrics. The final segmentation mean and standard deviation result in Jaccard similarity index, Dice similarity score, sensitivity and specificity are 0.8569 ± 0.0896, 0.9186 ± 0.0638, 0.9480 ± 0.0402 and 0.9917 ± 0.0387 respectively. Quantitative and qualitative segmentation result indicates the potential of the proposed framework.

Key words: **Brain tumor, Fuzzy Hopfield Neural Network, Segmentation, detection, MRI**

Acknowledgement

First of all, I would like to thank my advisor Dr. Eng. Getachew Alemu for his continuous support, encouragement and invaluable comments from initial proposal of this thesis research to the end.

I also would like to thank Dr. Abebe Mekonnen, radiologist at Pioneer Diagnostic Center, for providing brain MRI scans and for discussion we had. As well I would like to thank all staffs at Pioneer Diagnostic Center. Special thanks to Sir. Tigist Tadele for her help in screening and collecting brain MR images.

My special thanks for all Electrical and Computer Engineering staffs of AAiT for providing such a conducive environment throughout my study.

I also would like to thank my friends Ato Bizualem Tesfaye, Ato Berihun Kassaw, Ato Seifu Girma, Ato Melaku Fekadu and all my classmates for the time we had together.

Finally, I sincerely thank my parents for their constant love, support and encouragement.

Contents

List of Figures

List of Tables

Acronyms and Abbreviations

2D	Two Dimensions
3D	Three Dimensions
CAD	Computer Aided Diagnosis
CHNN	Competitive Hopfield Neural Network
CNS	Central Nervous System
CSF	Cerebrospinal Fluid
CT	Computed Tomography
DICOM	Digital Imaging and Communications in Medicine
DSS	Dice Similarity Score
DT	Decision Tree
DWT	Discrete Wavelet Transform
FCM	Fuzzy C-Means
FHNN	Fuzzy Hopfield Neural Network
FSE	Fast Spin Echo
GM	Gray Matter
HNN	Hopfield Neural Network
HSOM	Hierarchical Self Organizing Map
IARC	International Agency for Research on Cancer
IBSR	Internet Brain Segmentation Repository
iid	independent identically distributed
JSI	Jaccard Similarity Index

KNN	K-Nearest Neighbors
MI	Mutual Information
MLP	Multiple Layer Perceptron
MR	Magnetic Resonance
MRI	Magnetic Resonance Imaging
NN	Neural Network
PDC	Pioneer Diagnostic Center
PET	Positron Emission Tomography
PNG	Portable Network Graphics
RDWT	Redundant Discrete Wavelet Transform
RF	Radio Frequency
SE	Spin Echo
SOM	Self Organizing Map
SPECT	Single Photon Emission Computed Tomography
SVM	Support Vector Machine
T1	Spin-lattice relaxation time
T1-w	T1- weighted
T2	Spin-spin relaxation time
T2-w	T2- weighted
TE	Echo Time
TR	Relaxation Time
WHO	World Health Organization

WM	White Matter
ρ	Proton density

Chapter 1

Introduction

1.1 Motivation

Brain tumor, which is one of the most common brain diseases, has affected and devastated many lives. According to International Agency for Research on Cancer (IARC) it is estimated more than 126,000 people diagnosed for brain tumor per year around the world with more than 97,000 mortality [3]. The statistics shows low survival rate of brain tumor patients even though brain tumor disease has been the center of attention of thousands of researchers for many decades, around the world. In recent years, researchers from different disciplines ranging from medical to mathematical and computer sciences have combined their knowledge and efforts to better understand the disease and to find more effective treatments.

Magnetic resonance (MR) imaging and computed tomography (CT) scan of head are the most common tests taken to confirm presence of a brain tumor and identifying its location for selecting treatment options. Currently there are different treatment options for a brain tumor which includes surgery, radiation therapy, and chemotherapy. Treatment options and recommendations depend on several factors, including the size, type, and grade of the tumor, if it is putting pressure on vital parts of the brain, whether it has spread to other parts of the central nervous system (CNS) or body, possible side effects and the patient's preferences and overall health [6].

Above all, accurate detection of the type of brain abnormality is highly essential for treatment planning in order to minimize the fatal results. Obtaining of accurate result can be improved by using computer aided diagnosis (CAD) systems. The basic concept of CAD is to provide a computer output as a second opinion to assist radiologists' image interpretation by improving the accuracy and consistency of radiological diagnosis and also by reducing the image reading time. But segmenting brain tumors is a very difficult task. In the first place, there are a large class of tumor types which have a variety of shapes and sizes [7]. Appearance of brain tumors at different

locations in the brain with different image intensities [6] is another factor that makes difficult automated brain tumor detection and segmentation.

In this thesis, we proposed a fast c-means based fuzzy Hopfield neural network based framework to detect and segment brain tumor boundaries from multi-modal MR images combined with other image processing techniques in order to enhance brain tumor region extraction and visualization process.

1.2 Background

In this section, we briefly overview brain anatomy and tumors, brain imaging using magnetic resonance imaging (MRI), characteristics of brain tumors under MR imaging, and some theory about machine learning and its contributions in diagnosis of diseases.

1.2.1 Medical Background

1.2.1.1 Brain Anatomy Overview

The human brain is a highly specialized organ. It serves as the control center for functions of the body and allows us to cope with our environment. Words, actions, thoughts, and feelings are centered in the brain. In this section we describe the tissue structure and anatomical parts of the brain that we need to know for the purpose of this thesis.

The brain consists of mainly two tissue types: gray matter (GM) and white matter (WM). Gray matter is made of neuronal and glial cells, also known as neuroglia or glia that control brain activity and the basal nuclei which are the gray matter nuclei located deep within the white matter. The basal nuclei include: caudate nucleus, putamen, pallidum and claustrum. White matter fibers are myelinated axons which connect the cerebral cortex with other brain regions. The corpus callosum, a thick band of white matter fibers, connects the left and right hemispheres of the brain [2].

The brain also contains cerebrospinal fluid (CSF) that consists of glucose, salts, enzymes, and white blood cells. This fluid circulates through channels (ventricles) around the brain and the spinal cord to protect them from injury. There is also another tissue called meninges which are the membrane covering the brain and spinal cord [2].

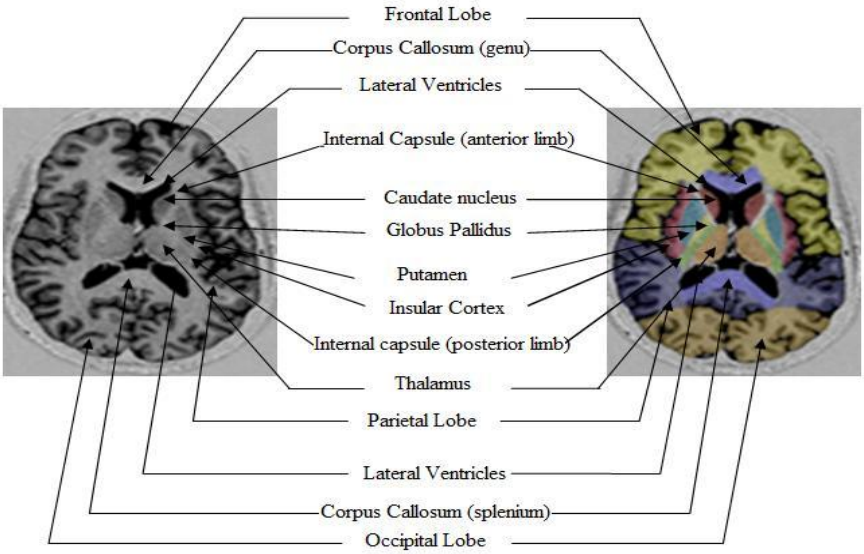

Figure 1.1 Overview structure of human brain, left side: an axial slice MR image, right side: the color coded version of image left side [69]

Anatomically the brain is composed of the cerebrum, the cerebellum and the brain stem as shown in Figure 1.2. The Cerebrum is the largest part of the brain and is associated with conscious thought, movement and sensation. It consists of two halves, the right and left cerebral hemispheres, each controlling the opposite side of the body. Each hemisphere is divided into four lobes: the frontal, temporal, parietal, and occipital lobes. The cerebellum is the second largest structure of the brain and is associated with controlling motor functions such as walking, balance, posture, and general motor coordination. It is located at the back of the brain and is connected to brain stems. Both, cerebrum and cerebellum have a thin outer cortex of gray matter, internal white matter and small, deeply situated masses of gray matter. The brainstem is located at the bottom of the brain and connected to spinal cord. It controls many vitally important functions

including motor and sensory pathways, cardiac and repository functions, and reflexes. It has three structures: the midbrain, pons and medulla oblongata [2].

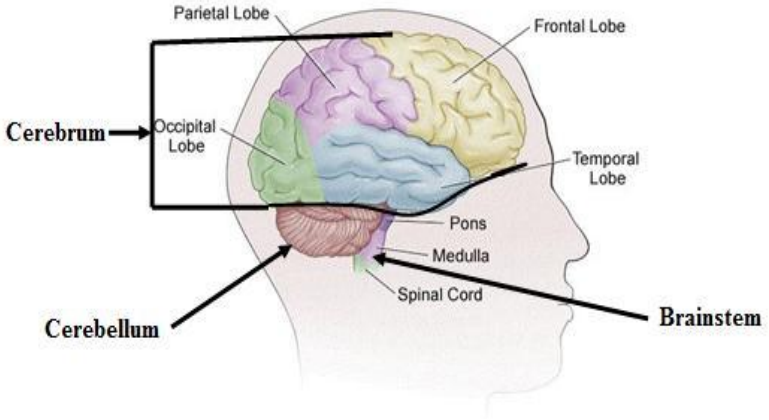

Figure 1.2 The major subdivision of human brain [69]

1.2.1.2 Brain Tumors

A brain tumor is an abnormal mass of tissue in which some cells grow and multiply uncontrollably, apparently unregulated by the mechanism that control normal cells. The growth of a tumor takes up space within the skull and interferes with normal brain activity. A tumor can cause damage by increasing pressure in the brain, by shifting the brain or pushing against the skull, and by invading and damaging nerves and healthy brain tissues [7].

Brain tumors are classified depending on the exact site of the tumor, the type of tissue involved, whether they are noncancerous (benign) or cancerous (malignant), site of origin (primary or secondary) and other factors [1]. According to World Health Organization (WHO), there are more than 120 types of brain tumors. The WHO classifies brain tumors by cell origin and how the cells behave, from the least aggressive (benign) to the most aggressive (malignant). Some tumor types are assigned a grade, ranging from Grade I (least malignant) to Grade IV (most malignant), which signifies the rate of growth; though there are variations in grading systems depending on the tumor type [7].

Primary brain tumors are the tumors that originated in the brain and are named for the cell types from which they originated. They can be benign (non cancerous) and malignant (cancerous). Benign tumors grow slowly and do not spread elsewhere or invade the surrounding tissues. However, growing in a limited space, a benign tumor can put pressure on the brain and compromise its function. On the other hand, malignant tumors grow quickly and can spread to surrounding tissues. Each of these tumors has unique clinical, radiographic and biological characteristics [7].

Secondary brain tumors originate from another part of the body. These tumors are actually composed of cancer cells from somewhere else in the body that have metastasized, or spread, to the brain. The most common cause of secondary brain tumors are: lung cancer, breast cancer, melanoma, kidney cancer, bladder cancer, certain sarcomas, and testicular and germ cell tumors [7].

1.2.2 MRI Brain Imaging and Characteristics of Brain Tumors

There are a variety of imaging techniques used to study brain tumors, such as: magnetic resonance imaging (MRI), computed tomography (CT), positron emission tomography (PET), single photon emission computed tomography (SPECT) imaging and cerebral angiography. In recent years, CT and MR imaging are the most widely used techniques, because of their widespread availability and their ability to produce high resolution images of normal anatomic structures and pathological tissues. Magnetic resonance imaging (MRI) is a method used to visualize pathological or other physiological alterations of living tissues and is commonly used for brain tumor imaging because of the following reasons [70].

- It does not use ionizing radiation like CT, SPECT and PET
- Its contrast resolution is higher than other techniques mentioned above
- Ability of MRI devices to generate 3D space images enables them to have superior tumor localization

- Its ability in acquisition of both functional and anatomical information about the tumor during the same scan.

Before discussing the MR image characteristics of brain tumors, it is important to describe the working principle of MR imaging. During MR imaging, the patient is placed in a strong magnetic field which causes the protons in the water molecule of the body to align in either a parallel (low energy) or anti-parallel (high energy) orientation with the magnetic field. Then a radiofrequency pulse is introduced which forces the spinning protons to move out of equilibrium state. When a radio frequency pulse is stopped, the protons return to equilibrium state and produce a sinusoidal signal at a frequency dependent on the local magnetic field. Finally, a radio frequency coils or resonators within the scanner detects the signal and creates the image [71].

When the resonator detects a signal under controlled condition, different images can be acquired and information related to tissue contrast may be obtained, revealing details that can be missed in other conditions. The amount of signal produced by specific tissue types is determined by their number of mobile hydrogen protons, the speed at which they are moving, and the time needed for the protons within the tissue to return to their original state of magnetization (T1) and the time required for the protons perturbed into coherent oscillation by the radiofrequency pulse to loose their coherence (T2) relaxation times. As T1 (spin-lattice) and T2 (spin-spin) relaxation times are time dependent, the timing of the radio frequency pulse and the reading of the radiated RF energy change the appearance of the image. The repetition time (TR) describes the time between successive applications of RF pulse sequences. The echo time (TE) describes the delay before the RF energy radiated by the tissue in question is measured. The pulse sequence, which is described by the TR and TE indicates the technique used to administer the RF energy, can be chosen to maximize the effect of differences in T1 or T2. This gives rise to the description of an MRI images as T1, T2 and proton density (ρ) weighted images. The T1-weighted images (short TR and short TE) provide better anatomical detail and, if used with contrast enhancement can provide anatomical and pathological details. The T2 weighted images (long TR and long TE) are sensitive to pathology. ρ weighted images (long TR and short TE), where number of protons per

unit volume in tissues is the main factor in determining formation of image contrast, shows anatomy and some pathology [71,72, 73].

There are two main MR imaging sequence families, depending on the type of echo recorded: spin echo sequence and gradient echo sequences. Spin echo (SE) sequence with its variant fast spin echo (FSE) sequence has been the standard MRI pulse sequences for anatomical and pathological details [73].

Brain images in MRI scan can be normal or abnormal. The normal brain is characterized by having gray matter (GM), white matter (WM) and cerebrospinal fluid (CSF) tissues. The abnormal brain usually contains active tumor, necrosis and edema in addition to normal brain tissues. Necrosis is a dead cell located inside an active tumor, while edema is located near active tumor borders. Edemas, which results from local disruption of blood brain barrier, often overlap with normal tissues and it is always difficult to distinguish [6].

The intensity values seen on an MRI scan for a particular brain depends primarily on the content of that pixel versus neighboring tissue and on other factors including the presence of abnormality. In normal brain MR images intensity level of brain tissues in the order of increasing brightness is CSF, GM, WM in T1-weighted (T1-w) and WM, GM and CSF in T2-weighted (T2-w) image, as shown in Figure 1.3.

In tumorous brain MR images intensity level of tumorous tissues exhibit different intensity level on T1-w and T2-w images based on the type of tumor. On T1-w most tumors have low or intermediate signal intensity but for some tumors this does not hold true, for example, glioblastoma multiforme tumor has high signal intensity. On T2-w most tumors have bright intensity but there are tumors which have low intensity, the classic examples are lymphoma tumors [6].

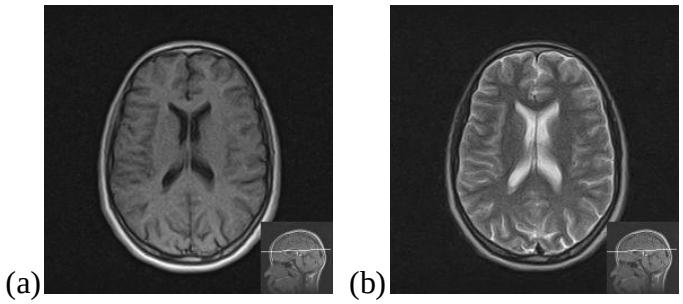

Figure 1.3 Original raw MRI data from Pioneer Diagnostic Center. a) T1-w axial scan image, b) T2-w axial scan image.

Data used in this thesis are axial T1-w and T2-w brain MRI scans. The performance of the proposed system has been experimented on the axial views of the MRI scans. Figure 1.4 shows some example of tumors intensity level characteristics in MRI.

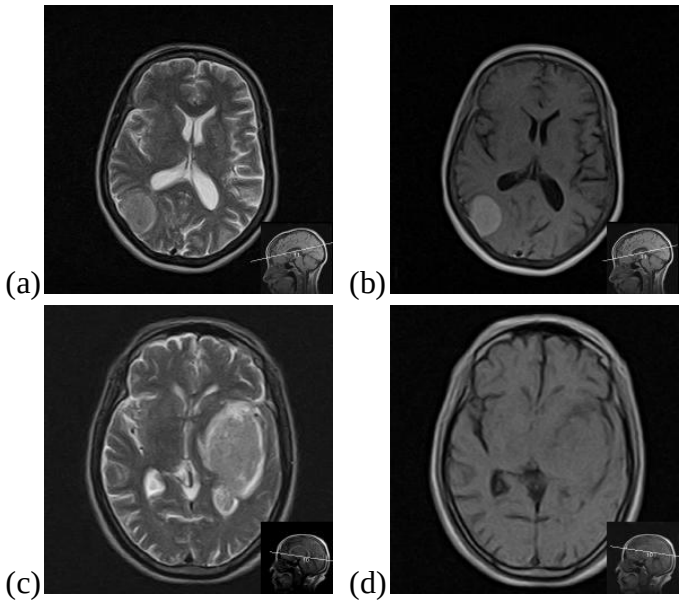

Figure 1.4 Tumor region intensity characteristics, Original raw MRI data from Pioneer Diagnostic center. (a) and (c) T2-w images, (b) and (d) T1-w images. Tumor region in a) low intensity, b) high intensity, c) high intensity and d) low intensity

1.2.3 Machine Learning

Machine learning is a branch of artificial intelligence that employs a variety of statistical, probabilistic and optimization techniques that allow computers to learn from past examples and to use that prior training to classify new data, identify new patterns or predict novel trends [74]. Machine learning has been the subject of tremendous interest in the biomedical community because it offers promise for improving the sensitivity and/or specificity of detection and diagnosis of disease. Recently, given the dramatic increase in medical data being collected, new diagnostic modalities being developed and the complexity of the data types and importance of multimodal analysis the need for automated system is greater than ever.

Traditionally used machine learning algorithms range from simple, probabilistic classifiers like Naïve Bayes [75], which once learned from existing data, classifies a new data instance by calculating the posterior probabilities of a hypothesis to more complex algorithms like Neural Networks that loosely simulate information processing by human brain, and that involve feed-forward and error propagation algorithms [74].

There are three main general types of learning in machine learning algorithms: supervised learning, unsupervised learning and reinforcement learning [75]. They are essentially classified on the basis of desired out-come of the algorithm. In supervised learning algorithms, such as Multi-Layer Perceptrons (MLP or NN), K-Nearest Neighbors (KNN), Support Vector Machine (SVM), Decision Tree (DT) to mention a few, the learning algorithm is given a labeled set of training data or examples. These labeled examples are the training set that the program tries to learn about or learn how to map the input data to the desired output. In unsupervised learning, a set of examples are given, but no labels are provided. Instead it is up to the learner to find the pattern or discover the groups. Unsupervised learning algorithms includes: Self-Organizing Maps (SOM), hierarchical clustering, K-means and fuzzy c-means clustering algorithms. In reinforcement learning, the learner is simply given a goal to achieve. The learner then learns how to achieve that goal by trial and error interaction with its environment. Reinforcement learning is

equivalent to standard supervised learning if the problem involves just two categories and equal cost of error [75].

For brain tumor detection and segmentation task from MR images supervised learning methods require labeled training data in their learning process which requires operator to define decision boundaries. This makes supervised methods to be operator dependent, which affects their reproducibility due to significant intra and inter observer variance introduced over multiple training samples. In addition to this, labeling the training data and the learning process takes much longer time. Also use of the same training set for a large number of scans can lead to biased results that do not take into account anatomical and physiological variability between different subjects.

On the other hand, in unsupervised methods the learning algorithm is simply provided with a set of data and automatically finds the structure in the data. This increases their desirability from reproducibility perspective and minimizing the learning time. In our case, we used unsupervised learning approaches to segment brain tumors from tumorous brain MR images.

In this thesis, the tumor detection and segmentation task is about finding out whether there is a pixel in an image with abnormal radiological property and separating the image into regions of similar attribute. The ultimate aim is to extract important features from the brain MR image data, from which a description, interpretation, or understanding of the scene can be provided. The algorithms and techniques used for tumor detection and segmentation are discussed in detail in chapter 3 and 4 of this paper.

1.3 Statements of the Problem

Manual segmentation and analyzing of MR brain tumor images by radiologists is reliable, but with no doubt it is tedious, time-consuming, highly subjective and impractical in today's medical imaging diagnosis where large numbers of images are taken for a single patient. As a result, there is strong demand to automate the tumor detection and segmentation process. Even though, there

are numerous efforts and promising results in the medical imaging community, accurate and reproducible segmentation and characterization of abnormalities using intelligent algorithms are still a challenging and difficult task because of the variety of possible shapes, locations and image intensities of various types of brain tumors. In this regard, this thesis focus on development of automated brain tumor detection and segmentation system that enhance detection and visualization of brain tumors from head MRI scans.

1.4 Objective of the Thesis

1.4.1 General Objective

In general, the objective of this thesis is to develop intelligent brain tumor detection, and segmentation and visualization system which in turn aid clinicians in diagnosis of brain tumor disease.

1.4.2 Specific Objectives

Specifically the aim of this thesis is:

- To identify the major difficulties that affect the efficiency of intelligent brain tumor detection and visualization systems starting from image acquisition to final visualization stage.
- To investigate the capability of multi-modal MRI images in brain tumor detection and segmentation.
- To propose a suitable preprocessing and hybrid machine learning algorithm which enhances the detection, and segmentation and visualization of tumor region of the brain.
- Finally, implement the proposed system in MATLAB and evaluate its efficiency with the most commonly used validation metrics.

1.5 Methodology

The methodology followed was:

- Literature was reviewed to explore the problem and possible solutions
- MRI scan of brain image data was collected from different sources that includes simulated and real, normal and tumorous datasets
- Designing of brain tumor detection and segmentation framework was performed
- The designed framework is implemented and simulated on MATLAB 7.7 environment
- Finally, the proposed system performance is validated against ground truth using commonly used quantitative metrics

1.6 Thesis Organization

The remainder of the thesis is organized as follows: chapter two is a literature review part that discusses about some of state of the art machine learning based methods in brain tumor detection and segmentation. The third chapter presents the proposed tumor detection and segmentation framework. This chapter presents a brief discussion on the first two modules, preprocessing and initial tumorous slice detection, of the proposed frame work. Similarly, chapter four provides a detailed discussion of the proposed hybrid intelligent machine algorithm, that is, fuzzy Hopfield neural network (FHNN). This chapter also presents the technique used to visualize the segmentation results.

Chapter five presents the results and validates the output of the proposed tumor detection and segmentation framework against ground truth using commonly used quantitative metrics. Also its presents some sample results for qualitative evaluation and discussion on the results. Finally, chapter six concludes the thesis and presents ideas for future work and improvements to the proposed system.

Chapter 2

Related Works

2.1 Introduction

Automatic detection and segmentation of brain tumor from brain MR images offer a mechanism for overcoming the tedium involved in the manual segmentation of large datasets. It also promises reproducibility which is affected by inter and intra observer variability. But automated systems have significant problems to achieve these objectives. The major problems are, pixel intensities violate the independent and identically distributed assumption within and between images due to the nature of brain MR images, and presence of a significant amount of artifacts and intensity inhomogeneity in MR images [29, 5]. Therefore, automated method should take into account these problems to achieve reproducible segmentation results and developing clinically accepted automated methods remains an active research area.

Many techniques have been proposed to automate the brain tumor detection and segmentation in recent years. The proposed methods can be broadly classified into two, intelligent based and non-intelligent based. Most notable intelligent based systems are artificial neural network, fuzzy c-means, support vector machine and hybrid methods. On the other hand, most notable non-intelligent methods include thresholding and region growing. But there is no clear demarcation between the two, especially intelligent based systems most often use the non-intelligent based ones as a refiner of their output. Some notable methods are reviewed in the following sections.

2.2 Thresholding Based Methods

Thresholding methods approach image segmentation based on gray level intensity value of pixels. A thresholding procedure attempts to determine an intensity value, called the threshold, which separates the desired classes. The segmentation is then achieved by grouping all pixels with intensity greater than the threshold into one class, and all other pixels into another class.

However, thresholding is often used as an initial step in a sequence of image segmentation process. Its main limitation is that in its simplest form only two classes are generated and it does not work when confronted with structures that lack clear borders. A survey on available thresholding techniques is provided on [9].

Most recently, thresholding based tumor detection and segmentation methods [13, 17] which integrated with watershed and histogram analysis have been proposed. But, these papers did not specify the data used for testing and validating their methods. Similarly, no quantitative result is provided.

2.3 Region Growing Based Methods

Region growing is a technique for extracting a region of the image that is connected based on some predefined criteria. In its simplest form, region growing requires a seed point that is manually selected by an operator, and extracts all pixels connected to the initial seed with the same intensity value. To eliminate the dependency on initial seeds and to make the method automatic statistical information and a priori knowledge can be incorporated in the algorithm. Region growing can also be sensitive to noise, causing extracted regions to have holes or even become disconnected. Conversely, overlapping gray value distribution in MR images can cause separate regions to become connected.

Region growing is not often used alone because it is not sufficient to segment brain structures accurately and robustly. In [18], region growing is integrated with boundary information by a level set technique. Where region growing is used as a propagation force and boundary information is used as a stopping criteria. The method is applied on a total of 246 axial tumor containing slices obtained from 10 patients and satisfactory results were achieved. But the method is semi-automatic as it relies on manual input seed region for region growing. More successful region growing is presented in [21]; the method needs precise anatomical information to locate initial seed pixels for each anatomical region and together with their associated

homogeneity. But the method's reliability depends on accuracy of the model assumption on homogeneity and region characteristics.

2.4 Neural Networks Based Methods

An artificial neural network is a biologically inspired computational model which consists of processing elements (called neurons) and connections between them with coefficients (weights), and training and recall algorithms attached to the structure. Nowadays, several types of neural networks have been designed and used in medical image segmentation and other fields. The multilayer perceptron and backpropagation learning algorithm (MLP), Hopfield neural networks (HNN) and self-organizing maps (SOM) neural network are some of the algorithms, to mention a few. A through treatment of neural networks can be found in [22]. Neural networks due to their ability of learning and generalization have attracted many researchers in image segmentation and for other image processing techniques [23].

One of the earliest applications of MLP to brain tumor segmentation is those of [26]. These studies were based on a training procedure that initially uses a single slice from a specific patient. With a training data set generated from this first slice, a MLP model was constructed and was used to segment the adjacent slice of this patient image set. The labels obtained from the adjacent slice were used to generate a second training data set, which was then used to segment the adjacent slice. This process continued until the entire available image data set was segmented. The proposed technique is semi-automatic, needs continues interaction with the user. Tumor segmentation accuracy is measured using Jaccard's similarity measure between areas delineated as a tumor by human expert and the proposed automatic methods achieved similarity index that varies from 0.6 to 0.78.

Kadam D. B. et al [16] have used eight textural features: angular second moment, contrast, inverse difference moment, sum variance, sum entropy, entropy, and difference entropy and information measure of correlation to train the MLP network in segmenting brain tumor. Although authors claim that their proposed method improves segmentation results, the qualitative

and quantitative results given are inadequate. In MLP supervised learning is achieved by assigning labels to each anatomical designation in the image, which has reproducibility and speed constraints as described in section 1.2.3.

Logeswari and Karnan in [27] used hierarchical self organizing map (HSOM), which is the extension of conventional SOM, to detect and visualize a brain tumor. Their system consists of two phases. In the first phase, the MRI brain image is preprocessed to remove artifacts then HSOM is applied for image segmentation. In this paper authors' highlighted the limitation of conventional SOM in which the number of neural units in the competitive layer needs to be approximately equal to the number of regions desired in the segmented image that is not possible to determine a priory the correct number of regions in the segmented image. The HSOM directly address the aforesaid shortcomings of the SOM. The performance of the system is measured in terms of weight vector, execution time and tumor pixels detected. But, the accuracy level of segmentation result is not given quantitatively and failed to distinguish the outer layer of the brain which is normally seen in MR brain images

In [31], Hopfield neural network is used to segment normal brain tissues and other medical images to their respective anatomical parts. They have used a modified version of HNN with integrated winner take all learning mechanism called competitive Hopfield neural network (CHNN). The computational efficiency of CHNN is high, but there is no guarantee on its optimal convergence, i.e., it may stuck to local minima.

2.5 Fuzzy Based Methods

After first introduction by Lofti zadeh, fuzzy logic has been used in several real world applications [22]. Fuzzy logic is a set of mathematical principles for knowledge representation based on degrees of membership rather than on crisp membership of classical binary logic. In brain tumor segmentation fuzzy systems permit the development of methods and algorithms that can perform tasks normally associated with intelligent human behavior.

In [34], expert knowledge and features derived from MR images are used to build fuzzy rules which are used to design fuzzy based tumor detection and segmentation. The system is fully automatic and exhibits unsupervised learning. To achieve this knowledge extraction was performed by means of intensity histogram analysis and a new method for obtaining membership functions to suit the MRI data is introduced. The detection and segmentation result obtained by this method is good, with the lowest score of 71% and the highest score of 93%, though experiment is performed only on two types of brain tumors, glioblastoma and meningioma multiform.

Another, very popular fuzzy based image segmentation is fuzzy c-means (FCM) clustering algorithm, which was first suggested by Dunn [35] and later improved by Bezdek et al [36]. Several researches have been done on implementing FCM and its improved versions for segmenting brain tumor from brain MR images.

In [33] region based fuzzy c- means clustering for brain tumor segmentation is proposed. The method uses the tumor class output of fuzzy clustering to initialize the region based algorithm, the region based moves towards the final tumor boundary. The method is validated for efficiency on 15 MR images where manual segmented ground truth is available. The result achieved is satisfactory having a Jaccard coefficient average value of 83.19% and sensitivity of 96.37%.

FCM clustering algorithm has been used to segment glioblastoma-multiform (GBM) brain tumors in [68]. Although the FCM algorithm is simple, fast and unsupervised, it cannot segment the tumor accurately because of the intensity overlapping of tissues and sensitivity of FCM to noise and initialization values. Their method is not validated and only tested for one case.

In [37],M.A. Jaffar et al. proposed an automatic brain MR image segmentation method using curvelet transform for noise removal and FCM for the automatic segmentation of brain MR images. In this paper the result of segmentation is given qualitatively and the effectiveness of the system towards tumor detection is not included.

Hsieh et al [8] used an algorithm integrating FCM and region growing techniques for automated tumor image segmentation from patients with meningioma. The accuracy and efficiency of the system is justified using percent match and correspondence ratio. The proposed systems overall percent match value was 72.80% $\pm$ 36.20% and the correspondence ratio value was 0.43% $\pm$ 0.86% but, if noticeable edema tissue existed within the image, the overall performance of the system would be degraded.

In [45], Indah Soesanti et al, proposed FCM algorithm that incorporates information about the summation of the membership function in the neighborhood of each pixel under consideration into the membership function for clustering. The paper emphasizes superiority of the method for noisy MRI brain images compared to other techniques, but the method is effective for relatively large tumor sizes ranging from 9.65 to 27.71 cm^2 and did not indicate the MR brain image data sources used in the experiment.

2.6 Hybrid Based Techniques

Hybrid system mix different methods of machine learning algorithms and make them work together to achieve a better solution to a problem, compared to using a single method for the same problem. The need of hybrid intelligence systems and their architecture is described in detail in [22].

A supervised hybrid fuzzy ANN based for tumor detection is proposed in [46]. The method is implemented in MATLAB and fuzzy back propagation algorithm (FBPA), hybrid architecture which maps fuzzy inputs to crisp outputs, is used to train the ANN. The result obtained using this supervised hybrid techniques is promising, but due to variability of image pixel intensities on different MRI scanners, different MR imaging modalities and effect of noise it is difficult to generalize the technique's efficiency.

A comparative study of adaptive network based fuzzy inference system (ANFIS), k-nearest neighbors (KNN) and fuzzy c-means (FCM) for brain tumor segmentation is conducted in [47].

The paper indicates for light abnormalities best segmentation performance is achieved by using ANFIS, whereas K-NN is good for dark abnormalities. The paper, as a future work, proposed integrating ANFIS, K-NN and FCM with other computer vision architectures will produce better segmentation results.

In [48], a fuzzy kohonen neural network is implemented for brain MR image segmentation. The technique used features like area, entropy, mean and standard deviation to segment tumor from brain MR image but did not use any preprocessing, for instance, noise removal to improve the extraction of these features. In addition, the qualitative and quantitative analyses given in this paper are inadequate.

In [49], fuzzy c-means strategy is integrated with HNN and introduced a fuzzy Hopfield neural network which is used for medical image segmentation. The method used the global histogram of images, in which frequency occurrence of each gray level used to construct the neurons. Consequently, the number of neurons is independent of image size. The experiment result is successful on normal axial brain MR images. But, for the objective functions to converge to a stable state it needs several synchronous iterations.

2.7 Other Brain Tumor Segmentation and Detection Techniques

There are methods that approach the brain tumor detection and segmentation in MRI using several parameters and techniques. Some of them are presented here. Automated brain tumor segmentation that has two phases is proposed in [19]. In first phase tumor is detected and initially segmented by a combination of histogram analysis, morphological operations and symmetry analysis. Then tumor is detected using fuzzy classification method or symmetry analysis and some morphological operations. There are two assumptions made in this method these are tumor appear in the image with specific gray level value and brain is roughly symmetrical. The method is validated on MR image volumes with cerebral tumors and manually segmented ground truth. The reported mean correct detection ratio (sensitivity) and Dice similarity score are 93% and 92% respectively.

In [44], a one support vector machine (SVM) is used for automatic brain tumor segmentation. SVM has advantage of generalization and working in high dimensional feature spaces. So it can learn the nonlinear tumor data distribution and optimally turn out a flexible decision boundary for the tumor region. In this framework, labeled image samples over the tumor areas must be feed to the one class SVM classifier for performing segmentation. Finally, the tumor segmentation is achieved by region based analysis. The method achieved acceptable result, but it needs continuous user interaction for the labeled samples. SVM classifier also used in [43] to classify tumor pixels based on feature vector generated from multi-parametric MR images. Then segmentation is done using levels set and region growing methods. To validate their proposed techniques MR images obtained from 11 subjects were used where tumor regions are manually delineated. The proposed method efficiency is compared with the manually delineated ground truth using Dice similarity score and the best performance obtained is a Dice similarity score of 0.69 with a standard deviation of ± 0.14. SVM have a limited accuracy because it treats image pixels as an independent and identically distributed.

Automated pediatric brain tumor segmentation that is based on Markov random field (MRF) model that combines probabilistic boosting trees (PBT) and lower level segmentation via graph cuts is used in [32]. Validation of the method is carried out on 6 multi-spectral MRI datasets where manually segmented truth is available. The reported segmentation result of this method is satisfactory, with Jaccard coefficients of 0.78 ± 0.17.

2.8 Summary

In this chapter we made a review on some notable and recent research work done on brain tumor detection and segmentation. Presenting all proposed methods on this paper is beyond a scope. This is due to the task to automate the brain tumor detection and segmentation from brain MR images is the most active research area and researchers have been publishing papers in alarming rate. Currently, there is no clinically accepted automated method to detect and segment brain tumors from MR images.

Chapter 3

Brain Tumor Detection and Segmentation Framework: Preprocessing and Tumorous Slice Detection

3.1 Introduction

In this thesis, a framework for an automatic brain tumor detection and segmentation based on fuzzy Hopfield neural network is proposed as shown in Figure 3.1. The proposed framework has three main components: image preprocessing, tumorous slice detection, and tumor segmentation and visualization.

In this chapter, we give an explanation for the preprocessing and tumorous slice detection of the framework of the proposed model. The preprocessing section performs intensity inhomogeneity correction, background noise removal and removes non brain tissues such as: skull and fat from head MRI scans. The second component of the framework, tumorous slice detection, performs image registration and interpolation to spatially align the two modalities of MR images used in this thesis. Fusion of the spatially aligned images is the next step in this second component of the framework. In third step, symmetry axis extraction is carried out on spatially aligned and fused MR images to identify the mid-sagittal plane of the brain. Finally, histograms of images to the right and left of the mid-sagittal plane are analyzed using Jeffrey divergence to initially identify the existence of tumor.

This chapter is organized as follows. Section 3.2 describes the artifacts in MRI and the image pre-processing method of the proposed framework. Section 3.3 describes the method used to initially detect the existence of tumor in the proposed framework that includes image registration, fusion and symmetry analysis. Also elaborates the need for fusion process and the metric used to evaluate the symmetry of the brain.

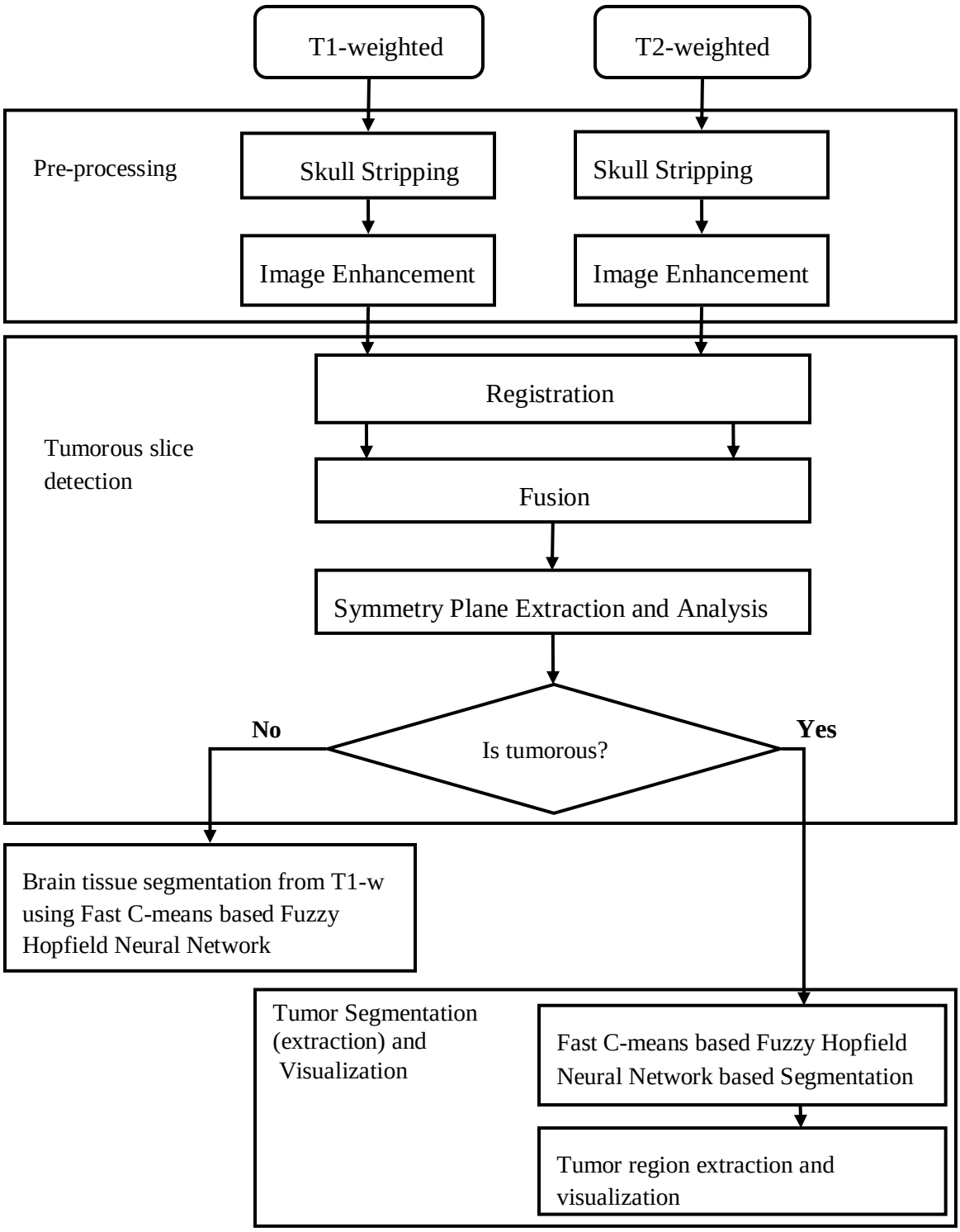

Figure 3.1 Framework of the proposed model

3.2 MRI Image Preprocessing

Artifacts in brain magnetic resonance imaging, are typically classified to patient-related (e.g. motion artifacts and metal artifacts), signal processing dependent (e.g. chemical shift artifacts, partial volume and wrapping around) and hardware related (e.g. RF noise, magnetic field inhomogeneity, RF inhomogeneity) depending on their origin. Most of the above artifacts can be eliminated during imaging and machine calibration [29]. The major sources of degradation of images in MRI are the sensitivity inhomogeneity of the receiver coils, coil tuning, gradient eddy currents, RF standing wave effects, and RF penetration effects. A common problem that arises due to these sources is intensity inhomogeneity (bias field), image corruption with a slowly varying multiplicative spatial field across the images. Intensity inhomogeneity is not always visible to human observer, but it causes significant tissue misclassification problems when intensity based segmentation is used [25]. Therefore, it is required to correct intensity inhomogeneity in the brain MR image prior to tumor detection and segmentation. Another essential step in enabling the processing of brain MR images is removing non brain tissues, skull stripping.

3.2.1 Intensity Inhomogeneity Correction

Image intensity inhomogeneity, also referred to as bias field, intensity non-uniformity or shading, consists of smoothly varying non-anatomical intensity variation across images. Its presence can significantly reduce the accuracy and reliability of quantitative and qualitative analysis of magnetic resonance (MR) images [25].

Various methods have been proposed for correcting intensity in-homogeneity in MR images. A review of a large number of intensity inhomogeneity correction methods can be found in [24], most of the methods are user dependent in order to tune a number of parameters that are used in the methods.

In this thesis, a local entropy minimization with a bicubic spline model introduced by [25] is used to correct severe intensity in-homogeneity in the MR images. The method uses bicubic spline to describe the bias field. The bicubic spline estimate of the bias field is optimized so as to minimize the entropy of the image using the piecewise, optimize and merge algorithms, which makes this method effective for severe intensity inhomogeneity in the images. In addition, the method used in [25] uses anisotropic diffusion filter to reduce other noise in the brain MR images.

3.2.2 Skull Stripping

Extraction of brain tissue from non brain tissues in MR images which is referred to as skull stripping is an important step in many neuro imaging studies. Several skull stripping methods have been proposed by different researchers [14, 28, 15].

Skull stripping algorithms can generally be categorized into four types: morphological based, deformable surface based, atlas based and hybrid based [28]. As indicated in [28, 15] skull stripping that uses intensity thresholding followed by morphological operations to remove narrow connections is the most common. But, this method first uses operator input to determine certain threshold value, the region of interest or a seed for a region growing phase which is error prone as operator might not provide appropriate input and time consuming.

In this thesis work we used automatic threshold value selection using Otsu's algorithm [39] to automatically choose threshold value. Then, mathematical morphology operations on a binarised image are applied stage by stage to achieve acceptable skull stripped brain images. The proposed skull stripping method comprises four steps as shown in Figure 3.2. Initially image binarisation is performed using threshold value obtained from Otsu's threshold selection algorithm and narrow connections are removed from binarised image using morphological opening. Then, largest connected component from binarised image is selected by considering the fact that brain is the largest connected structure inside the head. Thirdly, mathematical morphology operations such as: filling holes and dilation is carried out on selected largest binarised image. Finally, we

obtained skull stripped brain image using mathematical logical operations on binarised and original images. The above steps are described in more details in the following sections.

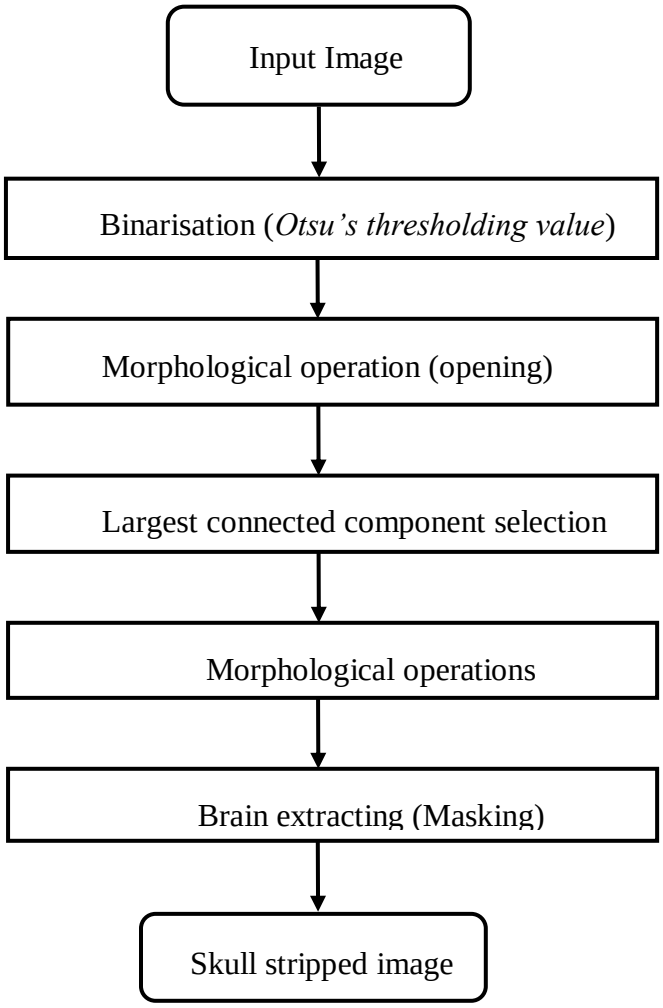

Figure 3.2 proposed skull stripping framework

3.2.2.1 Binarisation

Image binarisation is the simplest method of image segmentation that transforms an image gray level into only two values. By selecting optimum threshold value K^* it is possible to separate

brain MR image into two classes, one class is background: formed by the very low intensity pixels corresponding to air, part of cerebro-spinal fluid; and the other class is composed of foreground tissues including the gray matter (GM) and White matter (WM) of the brain as shown in the Figure 3.3b.

The main issue in image binarization is selecting optimum threshold value, K^*, in an image with a maximum gray level value of L . In this paper we used Otsu's algorithm [39] to automatically select threshold value. Otsu's algorithm uses the zeroth and the first order cumulative moments of gray level histogram.

The optimal threshold K^* that maximizes σ_B^2 (the criterion measure to evaluate the separability of the two classes; that is, background and foreground) is selected in the following sequential search.

$$\sigma_B^2(K) = \frac{[\mu_T \omega(k) - \mu(K)]^2}{\omega(K)[1-\omega(K)]} \dots\dots\dots\dots\dots\dots\dots\dots\dots\dots\dots\dots\dots\dots\dots\dots (3.1)$$

And the optimal threshold K^* is:

$$\sigma_B^2(K^*) = \max_{1 \le K \le L} \sigma_B^2(K) \dots\dots\dots\dots\dots\dots\dots\dots\dots\dots\dots\dots\dots\dots\dots\dots\dots\dots (3.2)$$

The range of K over which the maximum is sought can be restricted to [39]:

$$S^* = \{K: \omega_0 \omega_1 = \omega(K)[1-\omega(K)] > 0, or\ 0 < \omega(K) < 1\} \dots\dots\dots\dots\dots (3.3)$$

Where ω is class occurrence up to the K^{th} level, $\omega_0 = \omega(K)$ is class occurrence of background pixels with a range $[1, \cdots, K]$, $\omega_1 = 1 - \omega(K)$ is class occurrence of foreground pixels with a range $[K+1, \cdots, L]$, μ is class mean level up to K^{th} level, μ_T is the total intensity gray level mean value of the original image and σ_B^2 is between class variance.

3.2.2.2 Largest Connected Component Selection

Binarisation on brain MR images classifies the image into background and foreground, leaving the foreground into a number of connected components. By taking the assumption that brain is the largest connected structure inside the head we select the component whose area is the biggest. Figure 3.3c, shows the result of this operation.

3.2.2.3 Morphological Operations

Mathematical morphology is a theory of image transformations which is based on set-theoretical, geometrical, and topological concepts. Morphological operations implemented in this work include opening, dilation and filling. The two most common morphological operations, which are used as a base for all other morphological operations are: dilation and erosion [20].

Dilation operation makes the areas of foreground pixels grows in size, while reducing the holes with in those regions [20]. This is carried by moving a disk structuring element S on the binary image I.

$$I \oplus S = \{(x, y): S_{xy} \cap I \neq \emptyset\} \quad (3.4)$$

The dilation of I by S is the set of all image pixel points, (x, y), such that S and I overlap by at least one element.

Erosion operation makes the areas of foreground pixels shrink in size by eliminating irrelevant detail from binary image [20]. This is carried by moving a disk structuring element S on the binary image I.

$$I \ominus S = \{(x, y) : (S_{xy}) \subseteq I\} \quad (3.5)$$

This equation indicates that the erosion of I by S is the set of all image pixel points (x, y) such that S, translated by (x, y), is contained in I.

In this work first morphological opening which is applied before selecting the largest component selection breaks thin connections and removes thin protrusions. Opening operation on binarised image I by structuring element S is defined as [20]:

$$I \circ S = \left(I \ominus S_{xy}\right) \oplus S_{xy} \ldots\ldots\ldots\ldots\ldots\ldots\ldots\ldots\ldots\ldots\ldots\ldots\ldots\ldots\ldots\ldots\ldots\ldots\ldots\ldots\ldots\ldots .. (3.6)$$

As shown in equation (3.6), the opening I by S is the erosion of I by S, followed by a dilation of the result by S.

Then, dilation operation as given in equation (3.4) is performed on the image after largest connected component (brain image) is selected from earlier steps and results the image as shown in Figure 3.3d.

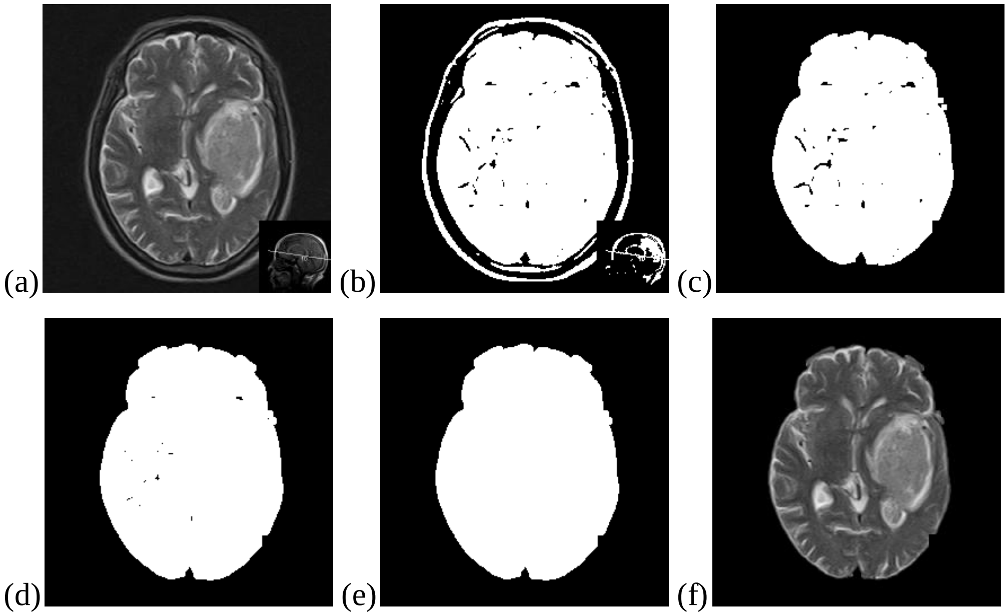

Figure 3.3 Original raw image from PDC dataset. Upper row from left to right: a) original axi-SE2D T1-w image, b) Binarised image, c) Largest connected component; brain image. Lower row from left to right: d) dilated e) mask; image after holes are filled f) skull stripped image

The final morphological operation performed in this work is the fill operation that is used to fill remaining holes in the binary image. Given a brain image region, I and initial point p of the holes region, region filling is done using equation (3.7) [20]. Figure 3.3e shows the result of this operation.

$$X_n = (X_{n-1} \oplus S) \cap I^c \qquad n = 1, 2, 3 \ldots\ldots\ldots\ldots\ldots\ldots\ldots\ldots\ldots\ldots\ldots\ldots (3.7)$$

Where $X_0 = p$, and S is the symmetric structuring element. The algorithm terminates at iteration step n if $X_n = X_{n-1}$.

3.2.2.4 Brain Extracting

The earlier steps enable us to obtain binary mask for head MRI scan as shown in the figure 3.3e. Then the brain is extracted by performing bitwise AND operation between the original head MRI scans, Figure 3.3a, with the binary mask, Figure 3.3e. This process also removes background noise and other non brain artifacts.

3.3 Tumorous Slice Detection

In this section, techniques used for detection of tumorous slice are elaborated. As indicated in section 1.2.2 brain tissues and pathologies in brain MR images under different imaging modalities have different gray level intensity values, different information. So, fusion of T1-w and T2-w images is carried out to acquire more descriptive images than any of the individual source images. For accurate fusion of images, the images to be fused must be registered to assure that the corresponding regions are aligned. Finally, symmetry analysis is used to detect the tumorous slice.

3.3.1 Image Registration

Image registration is the task of spatially aligning two images. A registration algorithm aligns two images by computing a transformation matrix that maps one image to the other, the second

image usually being a template. In this thesis, the T1-w images are used as a template in which the T2-w is spatially (geometrically) aligned and registration is performed on slice to slice basis.

An image registration framework can be better addressed by distilling the problem into four components: a feature extraction, similarity measure (feature matching), transformation model and image resampling and transformation (interpolation) [55].

The first step in image registration techniques is to decide image features used for matching. Accordingly, image registration techniques can be broadly classified into two categories: feature-based and intensity based. Feature based methods, which often use landmark points, line and surface in the images, requires segmentation and extraction of features from images, which makes this method data dependent. In addition, accuracy of registration algorithm is affected by the segmentation and feature extraction algorithms. On the other hand, intensity based image registration methods are free from this limitation because they do not deal with feature extraction but directly use the intensity feature of the images [12, 41].

Similarities between intensity features from template and floating image is measured in feature matching step. As indicated in [55, 12, 41], among existing intensity based image registration techniques mutual information based method is good in aligning multi-modality images accurately and robustly. Mutual information measures the degree of gray level value dependency between images. The mutual information (MI) of two images *R* and *F* can be defined in terms of the entropy *H(R)* and *H(F)* of the images, combined with their joint entropies $H(R,F)$ as: $I(R,F) = H(R) + H(F) - H(R,F)$. The dependency is assumed to be maximum when the images are matched [59].

In the third step, transforming the floating image to overlay it over the template image is carried out. Since registration is performed on T1-w and T2-w images of the same person it is reasonable to assume that head will not be deformed, and thus can be considered as a rigid body [60]. So, a rigid body transformation which consists of rotation (θ) and translation (t_x, t_y) is used in this paper.

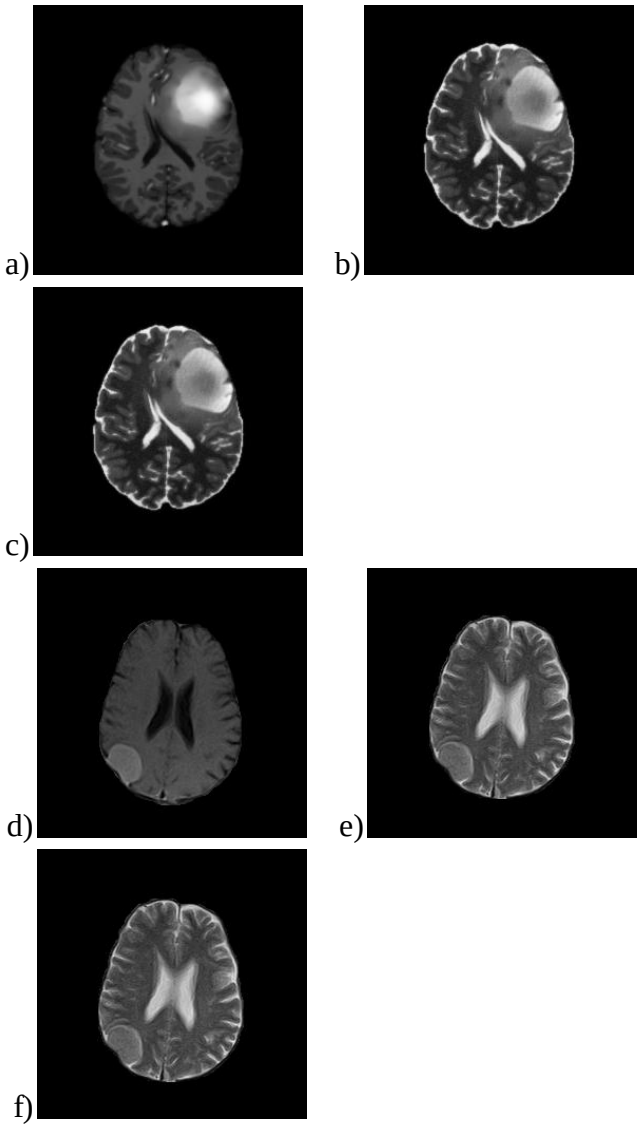

Figure 3.4 Registering T1-w and T2-w images. (a) and (d) T1-w images, (b) and (e) T2-w images, c) the registered T2-w image against (a). The estimated transformation parameters by the registering algorithms are $(-0.0073, -0.0990)$ for translation and $0.0101°$ for rotation, f) the registered T2-w image against (d). The estimated transformation parameters by the registering algorithms are (-0.8460, 2.0288) for translation and $-0.0339°$ for rotation. Note: $-\theta$ and θ represent clockwise and counter clockwise rotation, respectively. t_x and $-t_x$ represent to right and left translation, respectively. t_y and $-t_y$ to downward and upward translation, respectively.

Finally, image resampling (interpolation) is implemented on the floating image to eliminate artifacts (holes and/or overlaps) which resulted during rotation and translation of the floating image.

In this paper, rigid body image registration using maximization of mutual information implemented in [41] is used. As indicated in [41], to find maximum mutual information between the template and floating images Powell's direction set going along rotation and translation at each iteration by a series of tiny steps, 10^{-4}, is used. Figure 3.4 shows the result of image registration techniques used in this paper. Once the images are registered, the next step in the pipeline of the proposed framework is image fusion, which is discussed in the next section.

3.3.2 Image Fusion

Image fusion is the process of combining multiple input images into a single composite image, which contains a better description of the scene than the one provided by any of the individual input image. The composite image should therefore be more useful for human visual perception or for machine perception [61].

In MR brain imaging, T1-w and T2-w sequences produce different intensity levels for the same tissues as well as tumors. So, T1-w and T2-w images are fused to acquire more descriptive images than any of the individual source images. This in turn facilitates the tumor detection and segmentation processes. In a fused image, tumor region occupies highest gray level intensity values.

Image fusion can be performed at different levels of the information representation. According to [40] image fusion methods can be generally grouped into pixel level or sensor level, feature level and decision level. Pixel level fusion has advantage over the other methods due to originally measured quantities are used in pixel level fusion and algorithms are computationally efficient [40]. Pixel based fusion schemes range from simple averaging of registered images to more complex wavelet methods. Among methods reported in literatures discrete wavelet transform

based image fusion is the most common fusion method in medical images fusion due to its ability in retaining best spectral and spatial quality of fused image [10, 52, 40]. However, an important drawback to using the DWT in medical image fusion is the lack of shift invariance, which means a small shift in the input images create unpredictable changes in the energy distribution of the detail image pixels that leads to large distortion in the output. Redundant complex wavelet transforms (RDWT), undecimated version of the discrete wavelet transform, having properties of shift invariance and perfect reconstruction it is used to overcome the drawbacks of DWT in medical image fusion application [4].

RDWT works by suppressing the down-sampling step in the DWT. Because there is no down-sampling, the corresponding RDWT detail images and the approximation images have the same number of pixels as the input images. This property reduces image fusion process to a simple feature selection rule for combining the wavelets coefficients at each level [4, 38].

In this paper registered T2-w, i.e., outputs of registration operation as indicated in section 3.3.1, and T1-w brain MR images are fused using RDWT based image fusion. Let I^{T1} be T1-w and I^{T2} be T2-w images, and then fusion is carried out using the following steps:

1. Decompose the input images I^{T1} and I^{T2}, into a multi-resolution format using a redundant discrete wavelet transform. We use only one decomposition level, result is found good in a final fused image.

$$(I_a^{T1}, I_1^{T1}) = RDWT(I^{T1}) \quad \ldots\ldots (3.8)$$

$$(I_a^{T2}, I_1^{T2}) = RDWT(I^{T2}) \quad \ldots\ldots (3.9)$$

where: - $I_1^k = \left(H_1^k, V_1^k, D_1^k\right)$, $k = T1$ *or* $T2$ and *H, V and D* denote the horizontal, vertical and diagonal detail information respectively. I_a^{T1} and I_a^{T2} approximation images

2. Optimally fuse the approximation images I_a^{T1} and I_a^{T2}:

$$I_a^F = f(I_a^{T1}, I_a^{T2})\ ,\ I_a^F \text{- approximation band of fused image}$$

where we use the average of coefficients from approximation band, which preserves the features from both images [52].

3. Fuse the detail images I_1^{T1} and I_1^{T2}:

$$I_1^F = g(I_1^{T1}, I_1^{T2})\ ,\ I_1^F \text{- image fused from the three detailed sub-bands}$$

where $I_1^F = (H_1^F, V_1^F, D_1^F)$ is a fused image from the three detailed sub-bands *H, V* and *D* from both images. We use 3x3 block based entropy calculated from each respective sub-bands as a fusion operation decision criteria using equation (3.10) [52].

$$e_i^{jk} = ln\sqrt{\left(\frac{\mu_i^{jk} - \sum_{x,y=1}^{3,3} I_i^{jk}(x,y)}{\sigma_i^{jk}}\right)^2 / m^2} \ldots\ldots\ldots\ldots\ldots\ldots\ldots\ldots\ldots\ldots\ldots (3.10)$$

Where $j\ (= H, V, D)$ denotes the sub bands, $m = 3$ (size of each block), k represents the block number, and $i(= 1, 2)$ to differentiate the two multimodal images I^{T1} and I^{T2}. μ_i^{jk} and σ_i^{jk} are the mean and standard deviation of the RDWT coefficients of the k^{th} block of the j^{th} sub-bands from the i^{th} image respectively.

Then the detail sub-bands for the fused image $I_1^F = (H_1^F, V_1^F, D_1^F)$ are computed using the block that has maximum entropy from each multi-modal respective detail sub-bands. That is, for fused image block I_1^{Fjk}, RDWT coefficients from I^{T1} is selected if the entropy of block from I^{T1} image is greater than the corresponding block from the I^{T2} image, otherwise I_1^{T2jk} is selected.

$$I_1^{Fjk} = \begin{cases} I_1^{T1jk}, if\ \left(e_1^{jk}\right) > \left(e_2^{jk}\right) \\ I_1^{T2jk}, \qquad otherwise \end{cases} \quad \ldots\ldots\ldots\ldots\ldots\ldots\ldots\ldots\ldots\ldots\ldots\ldots (3.11)$$

Figure 3.5 shows sample result of the fusion operation.

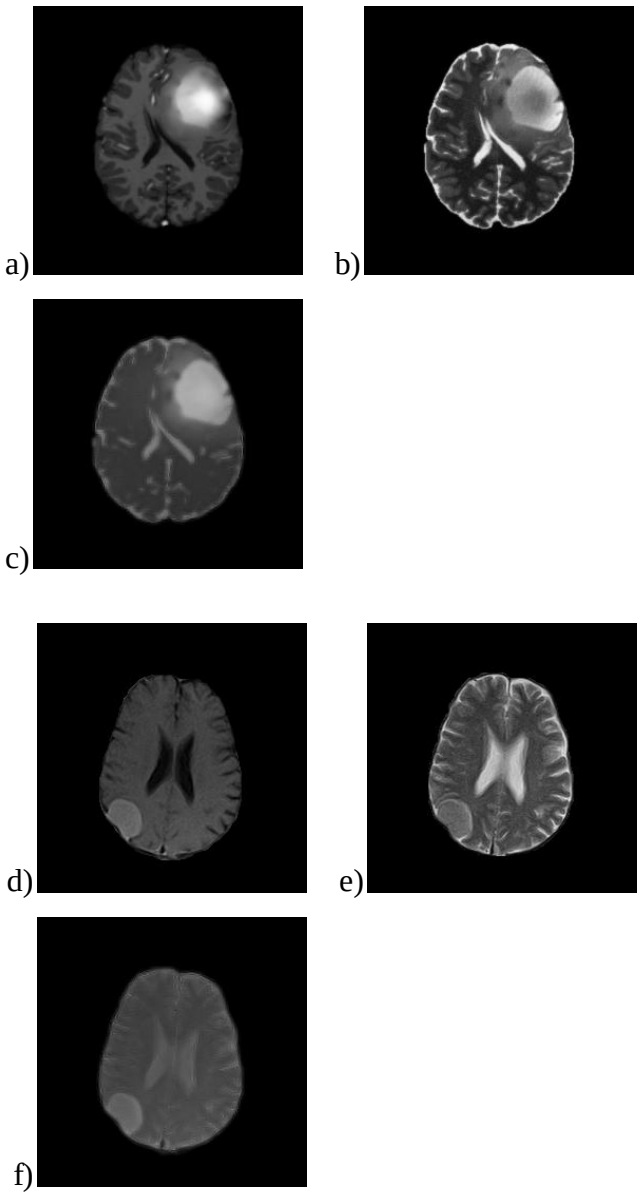

Figure 3.5 Fusion of T1-w and registered T2-w images. (a) and (d) are T1-w images, (b) and (e) are registered T2-w images, (c) and (f) are fused images

4. Finally, perform the inverse RDWT to obtain the fused image

$$I^F = RDWT^{-1}(I_a^F, I_1^F) \dots\dots\dots\dots\dots\dots\dots\dots\dots\dots\dots\dots\dots\dots\dots\dots\dots\dots.. (3.12)$$

3.3.3 Symmetry Analysis

The normal human brain can be divided into two hemispheres by an axis of symmetry and exhibit an approximate bilateral symmetry. Though the internal structure of a pathologic brain may depart from its normal bilateral symmetry, the ideal imaginary bilateral symmetry plane remains invariant [62, 63]. The axis of symmetry often referred to as mid-sagittal plane in literatures is defined as the plane separating both brain hemispheres and detection of this plane in MR brain images serve as a basis for the study of dissymmetry's in the brain hemispheres [64] and to detect abnormalities in the brain [65].

In this thesis, we analyzed abnormality of the brain based on symmetry analysis of image gray levels. Brain abnormalities show changes on brain MR images. Brain tumors producing mass-effect displaces and distort the surrounding structures; and infiltrating tumors affect the tissue characteristics, changing the intensity levels in the image. These characteristics can provide important information that tumors may be present [66]. Several works have been done to extract approximate symmetry plane [65, 63, 62, 67] but there is no best method for each cases of brain MR images as the methods are usually evaluated using different set of images most of them using normal brain images. In our case, the extraction of the approximate symmetry plane to separate the brain into the left and right hemispheres is performed by registering an image with its reflected version of itself. The method is implemented as follows.

First, we constructed a reflected image $F_i' = ref_V(F_i)$ by reflecting the image F_i about its vertical center line. Then using the registration technique described in section 3.3.1 registration of an image F_i with its reflected version F_i' is carried out. F_i', floating image, is rotated by angle θ using F_i as a template to maximize mutual information between the two images. As indicated in section 3.3.1 the tiny step taken for angle θ at each iteration is 10^{-4} in radian, that is, $0.0057°$.

After orientation θ has been obtained, we rotate an image F_i by an angle $\theta_f = -\theta/2$ so that its symmetry axis is vertically oriented. This is because F_i' to have maximum mutual information to F_i it would have to be rotated $2\theta_f$.

Finally, histograms of images to the right and left of symmetry axis is analyzed using Jeffrey divergence [34] as given in equation (3.13), to identify how much the symmetrical histograms diverge in the tumor gray levels.

$$d_j = (L, R) = \sum_i \left(l_i \log \frac{l_i}{m_i} + r_i \log \frac{r_i}{m_i} \right) \ldots\ldots\ldots\ldots\ldots\ldots\ldots\ldots\ldots\ldots\ldots\ldots (3.13)$$

where L and R are histogram of left and right hemisphere respectively and $m_i = \frac{l_i + r_i}{2}$

The abnormality changes the radiometric response of tissues and this affects the probability distribution of intensities in both hemispheres. By means of Jeffrey divergence it is possible to measure this dissimilarity [34]. Thus, we can suspect abnormality in cases with value of Jeffrey divergence measure greater than a certain threshold. After performing experiments on both normal and tumorous brain image it is found that for most tumorous cases the sum and normalized Jeffery divergence of all gray level values is above 0.0078. For most non-tumorous cases the sum and normalized Jeffery divergence of all gray level values lies in the range from 0.0011 to 0.0078. Ideally, the sum and normalized Jeffery divergence of all gray level values is zero for perfect similarity between left and right hemisphere according to equation 3.13. Figure 3.6 show some of the result of symmetry extraction and Figure 3.7 show the plot of Jeffery divergence of the right and left hemispheres of the gray level value of the images. The sum and normalized Jeffery divergence of all gray level values for JHC is 0.0011, for JHF is 0.0116 and for JHI is 0.0421. This implies Figure 3.6c is normal image, while Figure 3.6f and Figure 3.6i are suspected tumorous slice.

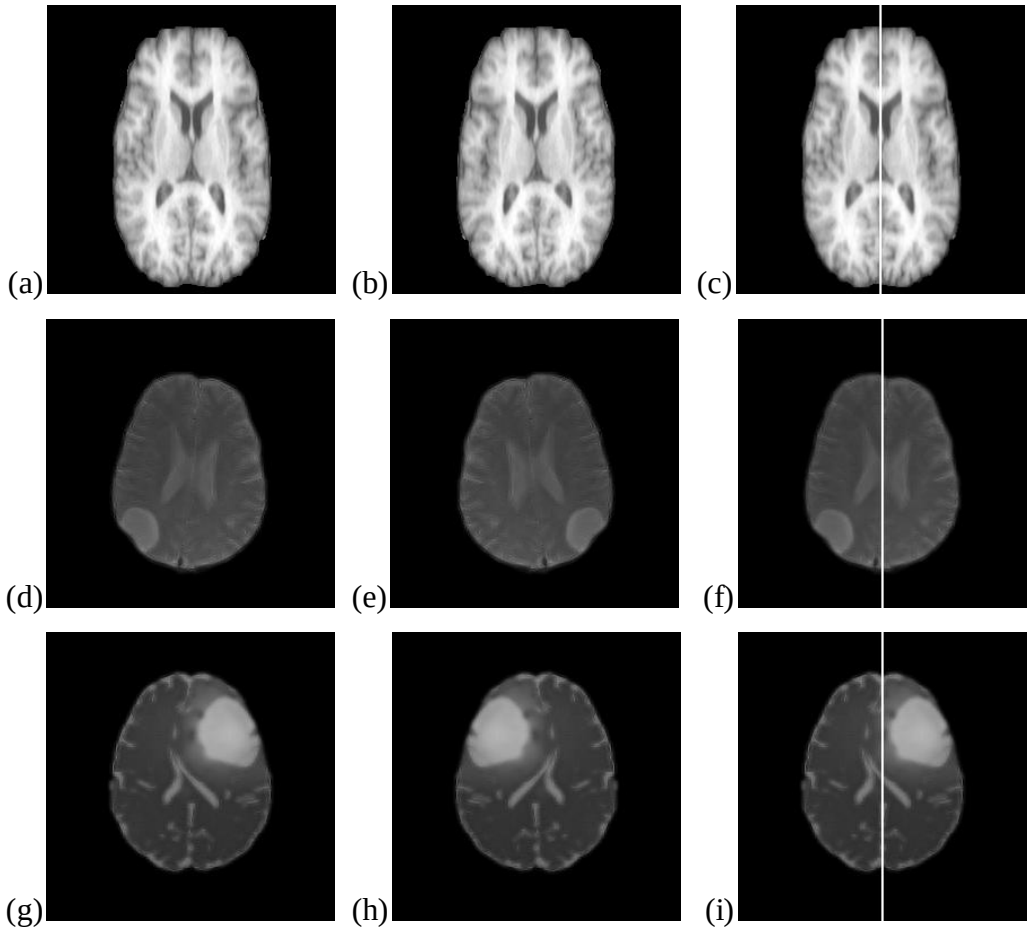

Figure 3.6 Extracted symmetry lines. Columns from left to right: First column, (a) T1-weighted normal simulated image, (d) T1-weighted and T2-weighted fused real tumorous image, (g) T1-weighted and T2-weighted fused simulated tumorous image. Second column, (b),(e) and (h) are reflected version of (a),(d) and (g) respectively. Third column (c), (f) and (i) symmetry plane extracted images by the proposed method

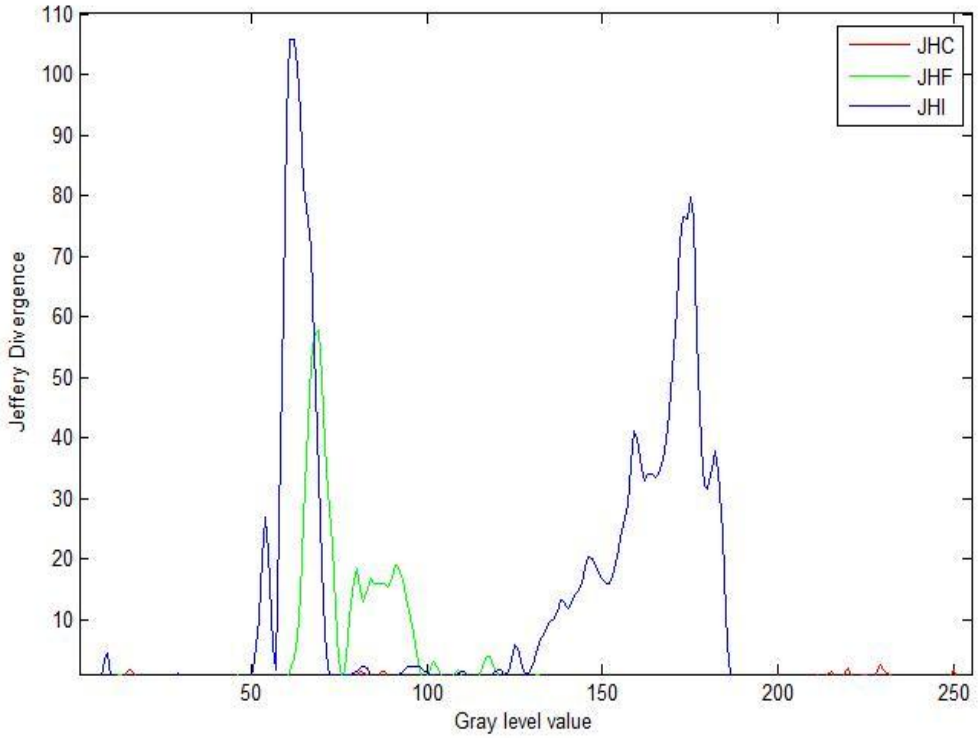

Figure 3.7 Jeffery diveregence histogram of the left and right hemispheres from extracted symmetry plane of: JHC- for image from Figure 3.6c, JHF- for image from Figure 3.6f and JHI- for image from Figure 3.6i.

Chapter 4

Brain Tumor Detection and Segmentation Framework: Tumor Segmentation and Visualization

4.1 Introduction

This chapter presents, the tumor segmentation and visualization section of our proposed framework. In this thesis, we implemented fuzzy Hopfield neural network based hybrid intelligent system for an automatic segmentation of brain tumors. The interesting properties of fuzzy Hopfield neural network are: first, It is among an unsupervised classification (clustering) techniques and it does not require user interaction, learning or prior models to perform segmentation task. Second, it is capable of making fuzzy clustering on the image where image pixels independent and identically distributed (iid) assumption fails which is common in brain magnetic resonance images [5]. Thirdly, it is computationally more efficient due to the inherent parallel structures.

This chapter is organized as follows: in section 4.2 fuzzy c-means and Hopfield neural network algorithms are described. Further the way in which fuzzy c-means is embedded into Hopfield neural network is elaborated. Then, in section 4.3 initial parameter selection to suit for the brain MR segmentation is presented. Finally, section 4.4 discusses the defuzzification and the way in which tumors are extracted.

4.2 The Proposed Fuzzy Hopfield Neural Network

In this section, first we introduce the fuzzy c-means and Hopfield neural network. Then we discuss the hybrid of the two algorithms, i.e. fuzzy Hopfield neural network.

4.2.1 Fuzzy C- means Clustering Algorithm

The conventional FCM algorithm is based on minimizing an objective function in the least squared sense. This section is briefed following [36].

Let c be number of clusters and is an integer in the range $1 < c < n$ and let $X = \{x_1, x_2, \dots, x_n\}$ denote a set of n unlabeled column vectors in space. X is numerical object data; in our case gray level intensity values of images has vector x_k as its numerical representation. Given X, we can say that c fuzzy subsets $\{u_{k,i}: X \to [0,1]\}$ are fuzzy c-partition of X if the nc values $\{u_{k,i} = u_k(x_i), 1 \le i \le c \; and \; 1 \le k \le n\}$ satisfy the following four conditions:

$$0 \le u_{k,i} \le 1 \qquad for\ all\ i,k \dots\dots\dots\dots\dots\dots\dots\dots\dots\dots\dots\dots\dots\dots\dots \quad (4.1)$$

$$\sum_{i=1}^{c} u_{k,i} = 1 \qquad for\ all\ k \dots\dots\dots\dots\dots\dots\dots\dots\dots\dots\dots\dots\dots\dots\dots \quad (4.2)$$

$$0 < \sum_{k=1}^{n} u_{k,i} < n \qquad for\ all\ i \dots\dots\dots\dots\dots\dots\dots\dots\dots\dots\dots\dots\dots\dots\dots \quad (4.3)$$

$$\sum_{k=1}^{n}\sum_{i=1}^{c} u_{k,i} = n \dots\dots\dots\dots\dots\dots\dots\dots\dots\dots\dots\dots\dots\dots\dots\dots \quad (4.4)$$

Each set of nc values satisfying the above equations can be arrayed as $n \times c$ matrix $= [u_{k,i}]$, membership function matrix. The element $u_{k,i}$ denotes the degree of possibility that an x_k belongs to an i^{th} fuzzy cluster. Then the FCM objective function can be written in the fuzzy c-prototypes as:

$$J_m(U, v; X) = \sum_{k=1}^{n}\sum_{i=1}^{c} (u_{k,i})^m \, D_{k,i}^2 \dots\dots\dots\dots\dots\dots\dots\dots\dots\dots\dots\dots\dots\dots\dots \quad (4.5)$$

Where $m \epsilon [1,\infty)$ is a weighting exponent on each fuzzy membership and it is fuzzification factor, $v = (v_1, v_2, \dots, v_c)$ are cluster centers, $D_{k,i}^2 = \|x_k - v_i\|^2$ is Euclidean distance between gray level intensity values of image's pixel x_k and cluster centers v_i.

The procedure of the fuzzy c-means algorithm is summarized in the following steps

1. Initialize the number of clusters c, initial cluster centers $\{v_i | \, i = 1,2, \dots, c\}$, the fuzzification parameter m and set $t = 0$. A detail about initialization of parameters is given in section 4.3.
2. Calculate membership matrix U for all points to all clusters using the following equation (4.6).

$$u_{k,i} = \left[\sum_{j=1}^{c} \left(\frac{\|x_k - v_i\|}{\|x_k - v_j\|} \right)^{2/m-1} \right]^{-1} \dots\dots\dots\dots\dots\dots\dots\dots\dots\dots\dots\dots\dots\dots\dots (4.6)$$

3. Update the new cluster center v_i using equation (4.7)

$$v_i = \frac{\sum_{k=1}^{n} (u_{k,i})^m x_k}{\sum_{k=1}^{n} (u_{k,i})^m} \dots\dots\dots\dots\dots\dots\dots\dots\dots\dots\dots\dots\dots\dots\dots\dots\dots\dots\dots\dots\dots\dots (4.7)$$

4. If $max_{k,i} \left\| u_{k,i}^{(t+1)} - u_{k,i}^{(t)} \right\| > \varepsilon$, then set $u_{k,i}^{(t)} = u_{k,i}^{(t+1)}$, set $t = t + 1$ and go to step 2; otherwise stop the process.

The fuzzification factor (m) controls the relative weights placed on each of the squared errors. If m is set to 1 then the algorithm reduces to crisp clustering algorithm. As $m \to \infty$ each entry of optimal membership matrix (U) approaches $1/c$, i.e., equal membership degree to all clusters. As a result for larger m the transition from a high membership degree from one cluster to the other is more smooth than for small m [36].

4.2.2 Hopfield Neural Network (HNN)

Hopfield neural network is a recurrent neural network in which all neurons are connected to each other, with the exception that no neuron has any connection to itself as shown in Figure 4.1. HNN with its simple architecture and parallel implementation [56] potential has been applied on numerous application areas, some of them include: image and speech processing, control, database retrieval, fault- tolerant computing, pattern classification and recognition, and automatic target recognition [42], to mention a few.

Hopfield neural network is a well known technique used for solving optimization problems based on the Lyapunov energy function. In our case two-dimensional Hopfield neural network consisting of $n \times c$ neurons which are fully interconnected is used, where c represents a class and n represents image pixels in a proper class. This section is briefed following [49].

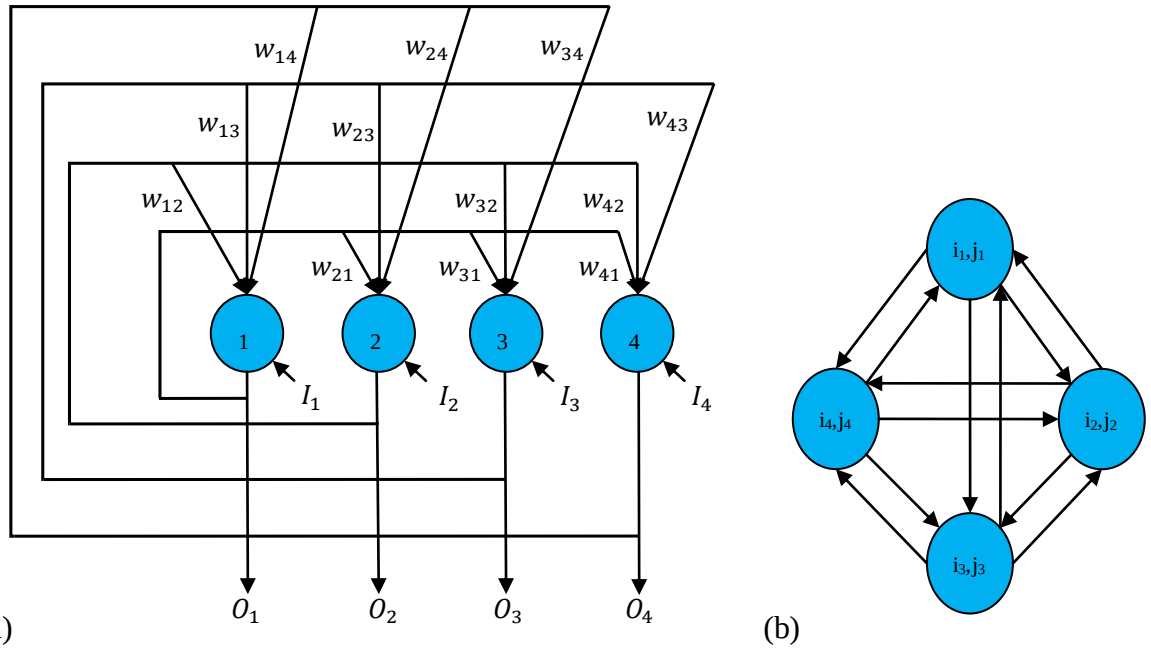

Figure 4.1 Hopfield neural network neuron interconnection, a) shows a view of neuron connection on a single plane b) shows the two-dimensional view of neurons interconnection

Let $V_{q,j}$ is a binary states of neuron (q,j) and $W_{k,i;q,j}$ be the interconnection weight between neuron (k,i) and neuron (q,j). A neuron (k,i) receives each neuron(q,j) with $W_{k,i;q,j}$ and a bias $I_{k,i}$ to yield the total weighted input $Net_{k,i}$ as given in equation (4.8):

$$Net_{k,i} = \sum_{q=1}^{n}\sum_{j=1}^{c} W_{k,i;q,j}V_{q,j} + I_{k,i} \dots\dots\dots\dots\dots\dots\dots\dots\dots\dots\dots\dots\dots\dots\dots\dots\dots\dots (4.8)$$

Where n is the number of data points (image pixels) and c is number of clusters. The Lyapunov energy function of two dimensional Hopfield neural networks is given by equation (4.9).

$$E = -\frac{1}{2}\sum_{k=1}^{n}\sum_{q=1}^{n}\sum_{i=1}^{c}\sum_{j=1}^{c} V_{k,i}W_{k,i;q,j}V_{q,j} - \sum_{k=1}^{n}\sum_{i=1}^{c} I_{k,i}V_{k,i} \dots\dots\dots\dots\dots\dots\dots . (4.9)$$

The network reaches a stable state, when the Lyapunov energy function is minimized.

The quality of classification result of Hopfield neural network is very sensitive to the weighting factors in the energy function [49]. Therefore, fuzzy reasoning is embedded into Hopfield neural network to eliminate the need for finding weighting factors in the energy function. In [11], Farhad M. et al. proposed a robust FHNN that embed fuzzy c-means with Hopfield neural network, for non-medical image segmentation. In this paper, their algorithm is extended for application to medical image segmentation, that is, brain tumor segmentation. FHNN is briefed in the next section.

4.2.3 Fuzzy Hopfield Neural Network

Hybridization of fuzzy c-means and Hopfield neural network gives feasible online learning and parallel implementation for image segmentation. [11], proposed a new approach which includes new objective function, and its minimization by Lyapunov energy function based on unsupervised two dimensional fuzzy Hopfield neural network. This new objective function consists of average distance between image pixels and cluster center. Also, the number of

neurons in the proposed FHNN is dependent on image size, i.e., for $n = L \times L$ image size and class number c the FHNN consists of $n \times c$ neurons that can be conceived as a two-dimensional array where each column (c) represents a class and each row (n) represents an image pixel in a proper class. This implies each pixel in the image is represented by c neurons in FHNN.

In FHNN, the total weighted input for neuron (k, i) and Lyapunov energy is modified as follows. Let $u_{q,i}$ be the fuzzy state of the $(q, i)^{th}$ neuron and $W_{k,i;q,i}$ represents the interconnection weight between neuron (k, i) and neuron (q, i). A neuron (k, i) in the network receives weighted inputs $W_{k,i;q,i}$ from each neuron (q, i) and a bias $I_{k,i}$ from outside. Then, the total input to neuron (k, i) is calculated using equation (4.10) [11]:

$$Net_{k,i} = \left[x_k - \sum_{q=1}^{n} W_{k,i;q,i} u_{q,i}^{m} \right]^2 + I_{k,i} \quad \ldots\ldots\ldots\ldots\ldots\ldots\ldots\ldots\ldots\ldots\ldots\ldots\ldots\ldots (4.10)$$

The modified Lyapunov energy function of the two-dimensional Hopfield neural network using FHNN strategy is given by equation (4.11) [11]:

$$E = \frac{1}{2} \sum_{k=1}^{n} \sum_{i=1}^{c} u_{k,i}^{m} \left[x_k - \sum_{q=1}^{n} W_{k,i;q,i} u_{q,i}^{m} \right]^2 - \sum_{k=1}^{n} \sum_{i=1}^{c} I_{k,i} u_{k,i}^{m} \quad \ldots\ldots\ldots\ldots\ldots (4.11)$$

where $\sum_{q=1}^{n} W_{k,i;q,i} u_{q,i}^{m}$ is the total weighted input received from neuron (q, i), $u_{k,i}$ is the output state at neuron (k, i) and m is the fuzzification parameter. Each column of this modified Hopfield network represents a class and each row represents an image pixel in the proper class. The network reaches a stable state when the modified Lyapunov energy function is minimal. For example, a neuron (k, i) in a maximum membership state indicates that pixel value of an image, x_k, belongs to class i.

In order to generate an adequate classification with constraints, the objective function is defined as given in equation (4.12) [11].

$$E = \frac{A}{2}\sum_{k=1}^{n}\sum_{i=1}^{c} u_{k,i}^{m}\left[x_k - \sum_{q=1}^{n}\frac{1}{\sum_{h=1}^{n} u_{h,i}^{m}} x_q u_{q,i}^{m}\right]^2 + \frac{B}{2}\left[\left(\sum_{k=1}^{n}\sum_{i=1}^{c} u_{k,i}\right) - n\right]^2 \quad \ldots\ldots (4.12)$$

The first term in equation (4.12) is the within-class scatter energy that is the Euclidean distance between samples to the cluster centroid over c clusters. The second term guarantees that the n data points (pixels) in an image can only be distributed among these c classes. More specifically, the second term imposes constraints on the objective function and the frist term minimizes the intra-class Euclidean distance from a sample to the cluster centroid in any given cluster.

Moreover, the quality of the classification results is very sensitive to the weighting factors A and B. Searching for optimal values for these weighting factors are time consuming and laborious. The FHNN can alleviate this problem so that the constraint terms can be handled more efficiently. In FHNN, all the neurons in the same row competes one another to determine which neuron has the maximum membership value belonging to class i. The summation of the membership grade of states in the same row equals 1, and the total membership states in all n rows equal n. That is, the network must match the constraints in equation (4.2) and (4.4). This ensures that all data points will be classified into c classes [11]. By using these constraints, the scatter energy of the FHNN in equation (4.12) can be simplified into equation(4.13).

$$E = \frac{1}{2}\sum_{k=1}^{n}\sum_{i=1}^{c} u_{k,i}^{m}\left[x_k - \sum_{q=1}^{n}\frac{1}{\sum_{h=1}^{n} u_{h,i}^{m}} x_q u_{q,i}^{m}\right]^2 \quad \ldots\ldots\ldots\ldots\ldots\ldots\ldots\ldots\ldots\ldots\ldots\ldots\ldots\ldots\ldots\ldots (4.13)$$

The minimization of energy E in equation (4.13) is greatly simplified since it contains only one term and hence the need to determine the weighting factors A and B vanishes. Comparing equation (4.13) with the modified Lyapunov function equation (4.11), the synaptic interconnection weights and the bias input can be obtained as equation (4.14) and equation (4.15) respectively.

$$W_{k,i;q,i} = \frac{x_q}{\sum_{h=1}^{n} u_{h,i}^{m}} \quad \ldots\ldots\ldots\ldots\ldots\ldots\ldots\ldots\ldots\ldots\ldots\ldots\ldots\ldots \tag{4.14}$$

$$I_{k,i} = 0 \quad \ldots\ldots\ldots\ldots\ldots\ldots\ldots\ldots\ldots\ldots\ldots\ldots\ldots\ldots\ldots\ldots\ldots\ldots \tag{4.15}$$

By substituting equation (4.14) and (4.15) into equation (4.10) the input to the neuron (k, i) can be expressed as in equation (4.16).

$$Net_{k,i} = \left[x_k - \sum_{q=1}^{n} \frac{1}{\sum_{h=1}^{n} u_{h,i}^{m}} x_q u_{q,i}^{m} \right]^2 = [x_k - v_i]^2 = D_{k,i}^2 \quad \ldots\ldots\ldots\ldots\ldots\ldots \tag{4.16}$$

From equation (4.16) we can infer that the cluster centroid is updated based on equation (4.17) as given below.

$$v_i = \sum_{q=1}^{n} \frac{1}{\sum_{h=1}^{n} u_{h,i}^{m}} x_q u_{q,i}^{m} \ldots\ldots\ldots\ldots\ldots\ldots\ldots\ldots\ldots\ldots\ldots\ldots\ldots\ldots \tag{4.17}$$

Accordingly, the state (membership function) of the neuron at the $(k, i)^{th}$ row, which is based on fuzzy c-means membership value computing technique in equation (4.6), is given in equation (4.18) as follows.

$$\mathrm{u}_{k,i} = \left[\sum_{j=1}^{c} \left(\frac{\mathrm{Net}_{k,i}}{\mathrm{Net}_{k,j}} \right)^{2/\mathrm{m}-1} \right]^{-1} \quad \ldots\ldots\ldots\ldots\ldots\ldots\ldots\ldots\ldots\ldots\ldots\ldots\ldots \tag{4.18}$$

The membership function represents the probability that a pixel belongs to a specific cluster and it is used to minimize the objective function in iteration. The new objective function consists of average distance between image pixels and cluster centroids for separate and compact clustering. The new objective function [11] is given in equation (4.19).

$$J = \frac{1}{N}\sum_{k=1}^{n}\sum_{i=1}^{c} u_{k,i}^{m} Net_{k,i} \ldots\ldots\ldots\ldots\ldots\ldots\ldots\ldots\ldots\ldots\ldots\ldots\ldots\ldots\ldots\ldots\ldots\ldots..\ldots..(4.19)$$

By using equation (4.16), (4.17), (4.18) and (4.19), the FHNN can cluster image pixels into c classes as described below.

Input: normalized fused MR brain image(x), cluster number c, fuzzification value (m), a norm inducing matrix (A) and termination tolerance $\varepsilon > 0$.

1. Compute primary centroids $v^{(0)}$
2. Compute initial distance between image pixels and primary centroids

$$D_{k,i}^{2} = \left\| x_k - v_i^{(0)} \right\| = (x_k - v_i)^T A (x_k - v_i) \ldots\ldots\ldots\ldots\ldots\ldots\ldots\ldots\ldots\ldots\ldots\ldots\ldots (4.20)$$

3. Compute initial membership value using equation (4.21)

$$u_{k,i}^{(0)} = \left[\sum_{j=1}^{c} \left(\frac{D_{k,i}}{D_{k,j}} \right)^{2/(m-1)} \right]^{-1} \quad \ldots\ldots\ldots\ldots\ldots\ldots\ldots\ldots\ldots\ldots\ldots\ldots\ldots\ldots\ldots\ldots\ldots\ldots..(4.21)$$

4. Compute new cluster centroid using equation (4.17)
5. Calculate the input to each neuron (k, i) using equation (4.16)
6. Compute the new membership value using equation (4.18)
7. Compute objective function value using equation (4.19)
8. If $\left| J^{(t+1)} - J^{(t)} \right| > \varepsilon$ go to step 4 , otherwise go to step 9
9. Defuzzification from final membership matrix.

4.3 Parameter Selection for FHNN

Several parameters such as: cluster number (c), fuzzification factor (m) and termination tolerance (ε) selection, and primary centroid computation is carried out before segmenting the brain MR image using FHNN.

Cluster number (c) is set to 5 to segment the tumorous brain image into (background, CSF, GM, WM and tumor) and set to 4 to segment non- tumorous brain image into (background, CSF, GM and WM) based on images pixel gray level intensity values.

Fuzzification parameter $m \in [1, \infty)$ determines the amount of fuzziness of the resulting segmentation. When $m = 1$ there will not be fuzziness in the clustering and leads to a crisp partition, in which $u_{k,i}$ is assigned either 0 or 1. As $m \to \infty$ the partition becomes completely fuzzy. In this case each entry of the final membership value($u_{k,i}$) equals $1/c$ [36]. However, a large m over emphasize the effects to a cluster from those data points which are far away from cluster centroid. In general, the fuzzifier m should be greater than 1 and cannot be too large. There is no theoretical basis for the optimal selection of m. But for most data, m in the range of $1.5 \leq m \leq 3$ gives good clustering result [36]. In the same manner to Farhad M. et al. [11], fuzzification parameter of $m = 2$ is used in this paper.

The shape of cluster is determined by the choice of the norm inducing matrix (A) in the distance measure. A common choice is $A = I$, where I is identity matrix, which gives the standard Euclidean norm [36].

The FHNN stops iterating when the norm of difference between objective functions (J) in two successive iteration is smaller than the termination parameter ε. The usual choice in literatures is $\varepsilon = 0.001$.

Brain MR images do not exhibit similar intensity level for all individual because of variability of anatomy and scanning machines. As a result, initial cluster centroid for each image must be

supplied to achieve good segmentation results. One way of doing this is manually initializing cluster center by the user, which is laborious and time consuming. In our case, to avoid user interaction initial cluster centroid is computed from global description of image's information which is acquired through histogram analysis.

Let, histogram of an image be represented by $h(i)$ and i is an integer representing image's gray level value in the range $[0,255]$. Then initial cluster centroids are initialized as follows.

First we perform histogram smoothing by one dimensional Gaussian filter to eliminate the parasitic peaks. Then the set of points $P_0 = (p_{0i}, h(p_{0i}))$ corresponding to the local maximums of the histogram are calculated using equation (4.22) [57].

$$P_0 = \{(i, h(i)) \mid h(i) > h(i-1) \,\&\, h(i) > h(i+1), \qquad 1 \leq i \leq 254\} \quad \ldots\ldots (4.22)$$

Then, repeating equation (4.22) on points of P_0 we get a new more significant local maximum points $P_1 = (p_{1i}, h(p_{1i}))$, as given in equation (4.23).

$$P_1 = \{(p_{0i}, h(p_{0i})) \mid h(p_{0i}) > h(p_{0i-1}) \,\&\, h(p_{0i}) > h(p_{0i+1}), \qquad p_{0i} \epsilon P_0\} \ldots\ldots (4.23)$$

The remaining peaks partitioned into required number of cluster needed for the segmentation. The maximum among the group is selected to be used as initial cluster centroid to initialize the fuzzy Hopfield neural network segmentation.

4.4 Tumor Visualization

When the iterative fuzzification stage becomes stable, all pixels in the image were considered belonging to one of the predetermined regions. The predetermined regions are background, CSF, GM and WM for the case of non-tumorous (normal) brain MR images and in the case of tumorous brain MR images predetermined regions are background, CSF, GM, WM and tumor. The process of visualizing the tumorous and normal tissue began by transforming the final

membership function matrix, $U = [u_{k,i}]$, back to the image by deciding to which region a gray level value x_k belongs, the process called defuzzification.

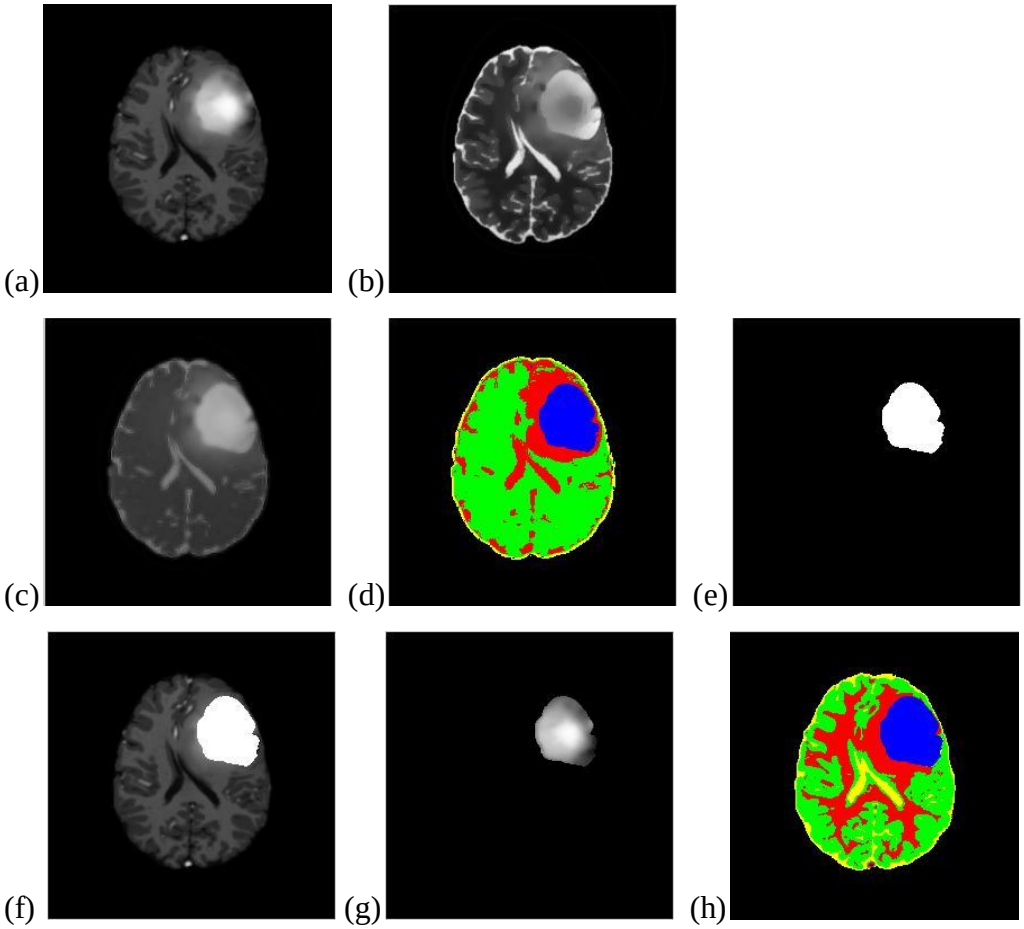

Figure 4.2 sample tumor extraction, and segmentation and visualization result of the proposed system. a) T1-w image, b) T2-w image, c) fused image, d) segmentation of fused image, e) Extracted tumor from (d), f) extracted tumor region superimposed on T1-w image using bitwise OR operation, g) extracted tumorous region part using bitwise AND operation, h) Final segmentation result to respective tissues CSF (yellow), GM (green), WM (red), Tumor (blue) and background (black).

In our case, the decision on how to assign x_k to a region (cluster) i was based on the winning $u_{k,i}$ having the highest value in the group, that is, $cluster_i = argmax\left(u_{k,i}\right) \forall i \, \epsilon \, c$. In doing so, x_k would be painted the same color code for region i, whereby the resulting images were classified by color-coded regions as shown in the Figure 4.2. Tissue class assignments after color coding is subsequently done by a human operator, who inspects the colored region and simply states "blue is tumor", etc.

Further, to improve the visualization of the tumorous region and other brain tissues we used the fused image as initial tumor segmentation, and then we extracted the tumor region output as shown in the Figure 4.2e and superimposed it into T1-w image as shown in the Figure 4.2f to refine segmentation. Finally we segment the tumor embedded T1-w image to its respective tissues (CSF, GM, WM and Tumor) and background as shown in the Figure 4.2h

Chapter 5

Simulation Data, Results and Discussion

5.1 Introduction

In this chapter, the tumor detection and segmentation framework which is described in chapter 3 and 4 is implemented in MATLAB, and the data used for experiments, the results and the challenges involved in assessing the performance of our implemented framework are described.

5.2 Challenges for Objective Validation of Tumor Segmentation Techniques

Validation and comparison of the performance of our proposed framework has been a challenging task due to lack of availability of existing implementation methods, data related issues and lack of standards to compare quantitatively the method with existing methods [19]. To obtain a consistent assessment of MRI brain tumor segmentation methods' performance and comparison, it is required to evaluate the various methods on a standard dataset. However, there is no dataset commonly available for this type of research. This is mainly due to confidentiality of patient scans and data privacy policies set by health institutions. As a consequence for the lack of a standard dataset, we tested our proposed framework on real MRI data obtained from Pioneer Diagnostic Center, real datasets of healthy brain MRI from IBSR [51] and simulated tumorous dataset obtained from [50].

For validation of our segmentation result we compared it with the manual segmentation of tumors as a ground truth. Manual labels are generally more accurate than automated segmentations of tumor volumes but are likely less consistent than automated labeling because of the error margin at the tumor boundary and because of human subjective interpretation of tumorous regions on brain MRI scans. In spite of these issues, several proposed tumor segmentation methods [34, 43, 32, 33, 19] use manually segmented data as a ground truth to measure the efficiency of their methods.

5.3 Experimental Data

Data used in this thesis are T1-weighted and T2-weighted head MRI scans and experiments have been done on the axial views of the MRI scans. We validated the proposed framework using three different datasets:

- Real tumorous brain MRI scans from Pioneer Diagnostic Center (PDC), Addis Ababa, Ethiopia
- Real normal (healthy) MR images from Internet Brain Segmentation Repository (IBSR) [51],
- Simulated tumor MR images [50].

The data obtained from pioneer diagnostic center includes MR images of 7 patients with different tumor types. The MRI protocol included:

- Axial Spin-echo T1-weighted (Axi-SE2D T1-w) imaging, with the following sequences:$TR/TE = 340000 - 600000ms/13000\,ms$, slice thickness $6mm$, size 256×256 pixels and with 14 axial slices on average for single patient.
- Axial Fast spin-echo T2-weighted (Axi-FSE2D T2-w) imaging, with the following sequences: $TR/TE = 4200000/100000\,ms$, slice thickness $6mm$, size 256×256 pixels and with 14 axial slices on average for single patient.

The medical images acquired from PDC were stored in a DICOM (Digital Imaging and Communications in Medicine) format which is the standard image format in the medical field and is used in storing MRI patients' scans. Each DICOM image file has both a header and a data file containing the stream of pixels. The header contains information about the patient, type of scan and image dimensions. We removed patient data from the DICOM header due to patient confidentiality issues. In addition, we converted the image volumes from the DICOM format to Portable Network Graphics (PNG) due to lack of portability of the DICOM format. For this purpose, we used MicroDicom to obtain PNG image slices for each of the scans by recursively

processing the subfolders of the patients. Segmentation ground truth is not provided for this data, but tumorous slice with patient record have been provided. Figure 5.1 shows sample images of PDC dataset with their tumor type.

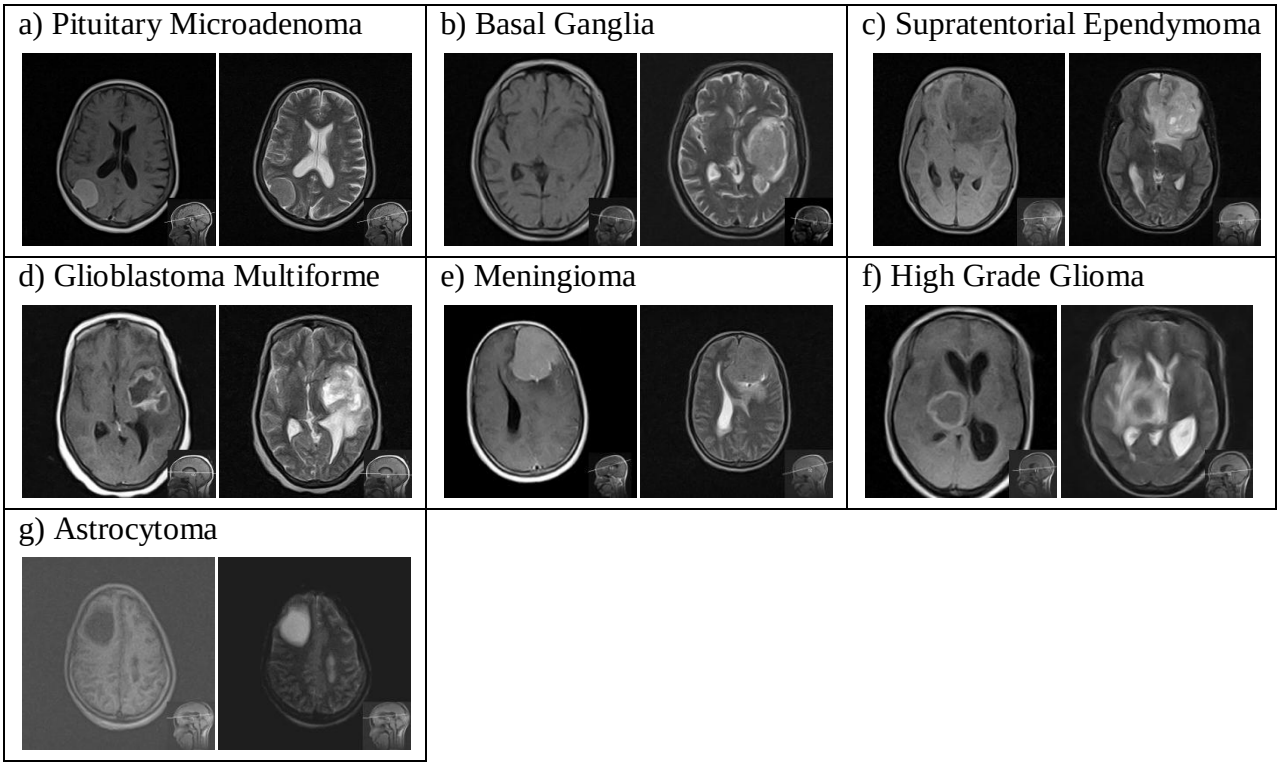

Figure 5.1 Brain MR Images obtained from Pioneer Diagnostic Center. a) T1-w (left) and T2-w (right) images of Patient A, b)T1-w (left) and T2-w (right) images of Patient B, c) T1-w (left) and T2-w (right) images of Patient C, d) T1-w (left) and T2-w (right) images of Patient D, e) T1-w (left) and T2-w (right) images of Patient E, f) T1-w (left) and T2-w (right) images of Patient F, g) T1-w (left) and T2-w (right) images of Patient G

IBSR's simulated healthy (normal) MR brain datasets and their manual skull stripped and segmented images were provided by the center of Morphometric Analysis at Massachusetts General Hospital [51]. The datasets contains 18 subjects, T1-weighted images with slice thickness of 1.5 mm, dimension of 256x256 pixels and on average 70 axial slice having Meta-Image (.hdr) data format. The image format is converted to PNG using freely availabe MRIcro

software for the same reason to PDC's images. We used the IBSR data to test the skull stripping efficiency of our proposed method.

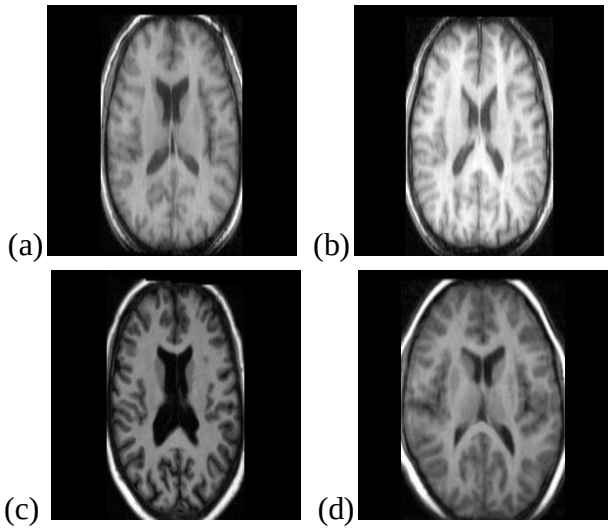

Figure 5.2 Healthy Brain MR images obtained from IBSR, T1-w image from subject a) IBSR_01, b) IBSR_06, c) IBSR_12, d) IBSR_18

Simulated tumorous brain MR image datasets and its ground truth were generated using the tumor simulation method discussed in [76, 77] and obtained from [50]. Simulation was performed using normal brain MR image. The simulated tumorous brain MR images datasets contains infiltrated and deformed tumors in T1-weighted and T2-weighted skull stripped axial slice images of 256x256 pixels dimension and on average 70 axial slices per subject. The file format of the simulated images is Meta-Image (.mha) file format and converted to PNG using image converter obtained from [54].

Figure 5.3 shows sample images of simulated tumor dataset with their tumor characteristics. The simulated tumor varies in size (small and big), location (edge and middle) and effect on normal tissues (displacement and infiltration). Displacing tumors produce mass-effect which distort the surrounding structure and infiltrating tumors affect the tissue characteristics, changing the intensity levels in the image.

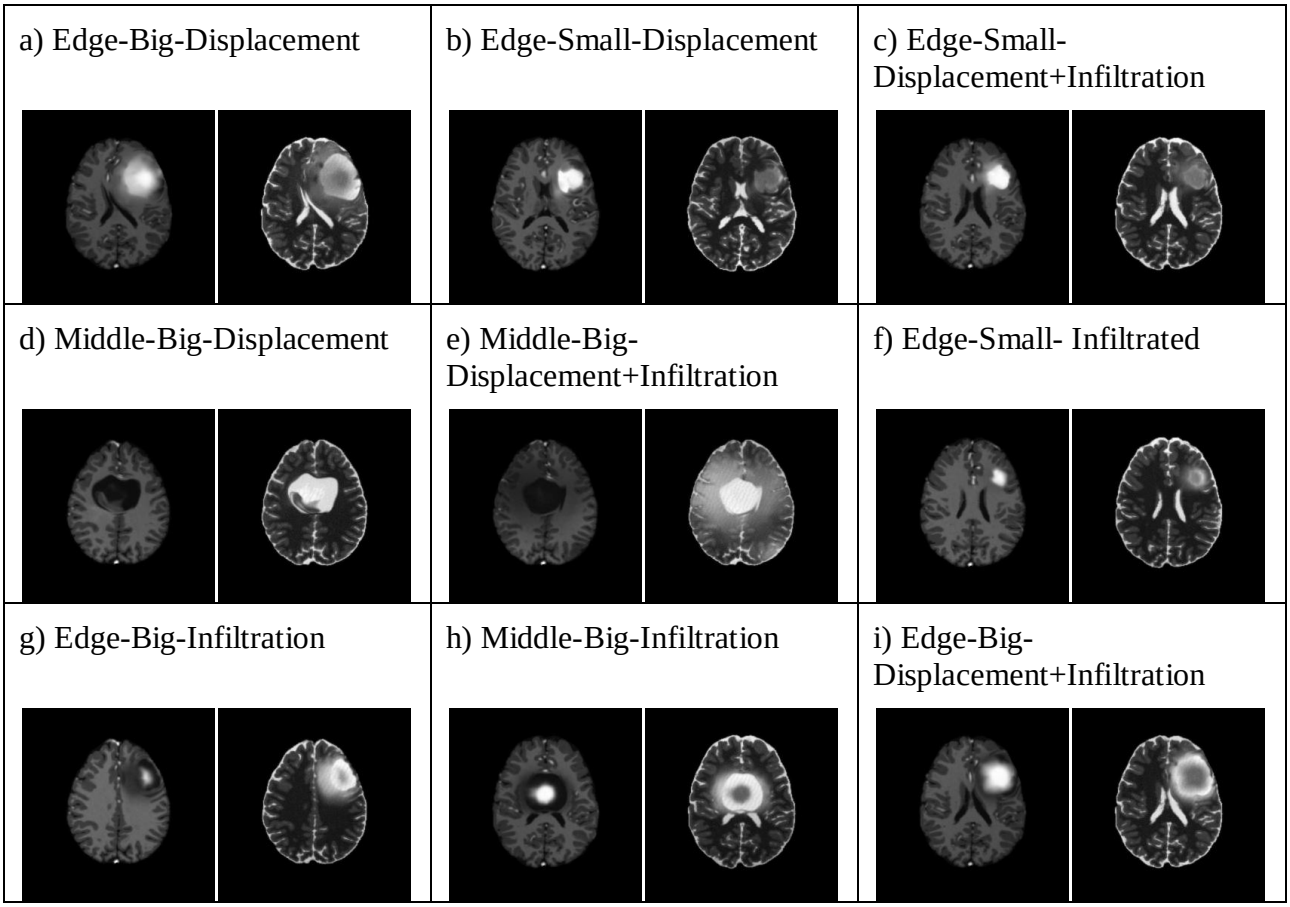

Figure 5.3 Simulated tumor MR images obtained from simulated tumor database. a) T1-w (left) and T2-w (right) images of S01, b)T1-w (left) and T2-w (right) images of S02, c) T1-w (left) and T2-w (right) images of S03, d) T1-w (left) and T2-w (right) images of S04, e) T1-w (left) and T2-w (right) images of S05, f) T1-w (left) and T2-w (right) images of S06, g) T1-w (left) and T2-w (right) images of S07, h) T1-w (left) and T2-w (right) images of S08, i) T1-w (left) and T2-w (right) images of S09

5.4 Performance Validation Metrics

We validate the performance of our skull stripping and tumor segmentation methods using the most commonly used validation metrics in literatures [34, 43, 32, 33, 65, 14] which includes: Jaccard similarity index (JSI) [58], Dice similarity score (DSS) [30], and specificity and sensitivity [53]. Validation is performed by comparing the proposed method's output with manually obtained ground truth. Let G_T be manually obtained ground truth and O_M be the output result of the proposed method. For skull stripping technique G_T and O_M are compared on a set pixels labeled as a brain by the ground truth and our proposed skull stripping method respectively. For tumor segmentation G_T and O_M are compared based on a set of pixels labeled as a tumor by the ground truth and our proposed method respectively.

The result of comparing O_M against G_T can have four possible outcomes.

- *True Positive*(T_P), where the O_M and the G_T both classified an image as brain, tumorous and tumor region for skull stripping, brain slice classification and tumor segmentation methods respectively. Mathematically $T_P = G_T \cap O_M$
- *True Negative*(T_N), where the O_M and the G_T both classified an image as non-brain, non-tumorous and non-tumor region for skull stripping, brain slice classification and tumor segmentation methods respectively. Mathematically $T_N = \overline{G_T} \cap \overline{O_M}$
- *False Negative*(F_N), where G_T classified an image as brain, tumorous and tumor region but the O_M classified an image as non-brain, non-tumorous and non-tumor region for skull stripping, brain slice classification and tumor segmentation methods respectively. Mathematically, $F_N = G_T \cap \overline{O_M}$
- *False Positive*(F_P), where O_M classified an image as brain, tumorous and tumor region but the G_T classified an image as non-brain, non-tumorous and non-tumor region for skull stripping, brain slice classification and tumor segmentation methods respectively. Mathematically, $F_P = \overline{G_T} \cap O_M$.

Based on these outcomes the metrics are defined as follows, Jaccard similarity index for two sets is defined as the size of intersection of the two sets divided by the size of their union as given in equation (5.1).

$$JSI = \frac{|G_T \cap O_M|}{|G_T \cup O_M|} = \frac{T_P}{(T_P + F_P + F_N)} \dots\dots\dots\dots\dots\dots\dots\dots\dots\dots\dots\dots\dots (5.1)$$

A Jaccard similarity index value of 1 indecates a perfect agreement between the two sets and 0 indicates no agreement between sets.

The Dice similarity score is defined as the size of intersection of the two sets divided by their average size as shown in equation (5.2).

$$DSS = \frac{|G_T \cap O_M|}{\frac{1}{2}(|G_T| + |O_M|)} = \frac{T_P}{\frac{1}{2}(2T_P + F_N + F_P)} \dots\dots\dots\dots\dots\dots\dots (5.2)$$

Both Jaccard similarity index and Dice similarity score measures the degree of overlap between G_T and O_M.

The sensitivity measures the fraction of true positives that are correctly detected and it is defined as in equation (5.3).

$$Sensitivity = \frac{T_P}{(T_P + F_N)} \dots\dots\dots\dots\dots\dots\dots\dots\dots\dots\dots\dots\dots (5.3)$$

The specificity measures the fraction of true negatives that are correctly detected. Specificity is defined as in equation (5.4).

$$Specificity = \frac{T_N}{(T_N + F_P)} \dots\dots\dots\dots\dots\dots\dots\dots\dots\dots\dots\dots\dots (5.4)$$

By evaluating the results of the above four validation metrics, we can conclude how the proposed method is efficient in skull stripping, tumor detection and segmentation in brain MR images when compared against ground truth.

5.5 Experimental Results and Discussion

5.5.1 Skull Stripping Performance Measure

After obtaining input images the first work is to remove non-brain tissues such as skull, fat and other imaging artifacts from MRI scans using the technique outlined in section 3.2.2 and intensity inhomogeneity correction using the method described in section 3.2.1. The efficiency and precision of skull stripping stage is highly important since subsequent stages in the pipeline of the proposed framework use the output of this stage. The skull stripping method is tested on IBSR and PDC datasets. The quantitative and qualitative visual results of skull stripping method are presented as follows.

Table 5.1 shows the result of the proposed skull stripping method on IBSR datasets. We calculated the Jaccard similarity index, Dice similarity score, sensitivity and specificity of the skull stripping result using manually obtained ground truth. Jaccard similarity index and Dice similarity score, measures how well the manually skull stripped ground truth overlap with our result. A score of 1.0 represents perfect overlap while 0.0 represents no overlap. Sensitivity measures how well the performance of skull stripping method is in avoiding removal of brain tissues together with non-brain tissues. On the other hand, specificity measures how well the performance of the method on not wrongly classifying non-brain tissues as brain tissues. Larger value of sensitivity indicates the more accurate the skull stripping method is. But, if in case the skull stripping technique includes non-brain tissues in the final result rather than avoiding them sensitivity remains high. So, sensitivity has to be coupled with specificity to measure the accuracy of the skull stripping method. Generally, an accurate and robust skull stripping technique must have good performance for all multiple performance metrics.

Table 5.1 *Mean (standard deviation)* value of Jaccard similarity index (JSI), Dice similarity score (DSS), sensitivity and specificity for IBSR datasets.

Data	JSI	DSS	Sensitivity	Specificity
IBSR_01	0.9378 (0.0170)	0.9678 (0.0092)	0.9918 (0.0053)	0.9663 (0.0073)
IBSR_02	0.9721 (0.0128)	0.9858 (0.0067)	0.9931 (0.0032)	0.9867 (0.0083)
IBSR_03	0.9563 (0.0370)	0.9773 (0.0210)	0.9781 (0.0226)	0.9906 (0.0119)
IBSR_04	0.9635 (0.0241)	0.9812 (0.0127)	0.9914 (0.0056)	0.9878 (0.0083)
IBSR_05	0.9310 (0.0502)	0.9635 (0.0282)	0.9906 (0.0087)	0.9742 (0.0143)
IBSR_06	0.9668 (0.0215)	0.9830 (0.0113)	0.9888 (0.0032)	0.9834 (0.0186)
IBSR_07	0.9554 (0.0319)	0.9769 (0.0176)	0.9754 (0.0020)	0.9925 (0.0020)
IBSR_08	0.9039 (0.0657)	0.9482 (0.0414)	0.9639 (0.0427)	0.9702 (0.0160)
IBSR_09	0.8843 (0.0839)	0.9300 (0.0499)	0.9517 (0.0341)	0.9686 (0.0412)
IBSR_10	0.8632 (0.1487)	0.9187 (0.1004)	0.9407 (0.0798)	0.9610 (0.0619)
IBSR_11	0.9200 (0.0791)	0.9564 (0.0460)	0.9912 (0.0047)	0.9590 (0.0485)
IBSR_12	0.8437 (0.1742)	0.9046 (0.1142)	0.9762 (0.0123)	0.9130 (0.1214)
IBSR_13	0.9699 (0.0138)	0.9847 (0.0072)	0.9981 (0.0013)	0.9873 (0.0028)
IBSR_14	0.9636(0.0309)	0.9812 (0.0165)	0.9950 (0.0118)	0.9852 (0.0092)
IBSR_15	0.9438 (0.0603)	0.9700 (0.0340)	0.9920 (0.0149)	0.9701 (0.0291)
IBSR_16	0.9540 (0.1414)	0.9760 (0.0226)	0.9893 (0.0035)	0.9758 (0.0276)
IBSR_17	0.9598 (0.0413)	0.9790 (0.0223)	0.9949 (0.0023)	0.9737 (0.0311)
IBSR_18	0.9566 (0.3100)	0.9776 (0.0163)	0.9795 (0.0113)	0.9827 (0.0193)
Average	0.9359 (0.0747)	0.9645 (0.0321)	0.9823 (0.0150)	0.9738 (0.0266)

From Table 5.1 we can observe that the skull stripping results are at an acceptable level, even to datasets where there is weak connection between brain tissues and darker intensities at the brain boundary for example the case of IBSR_12. Also the sensitivity of the method is in average well above 98%. Having higher sensitivity is more important to avoid removal of brain tissues, which is critical for accuracy of subsequent stages.

Qualitatively skull stripping methods can be evaluated by the size of remaining non-brain tissues in the skull stripped image and the extent of brain tissues loss in the stripped image. Qualitatively Figure 5.4 and 5.5 show the result of skull stripping by proposed method on IBSR and PDC datasets respectively.

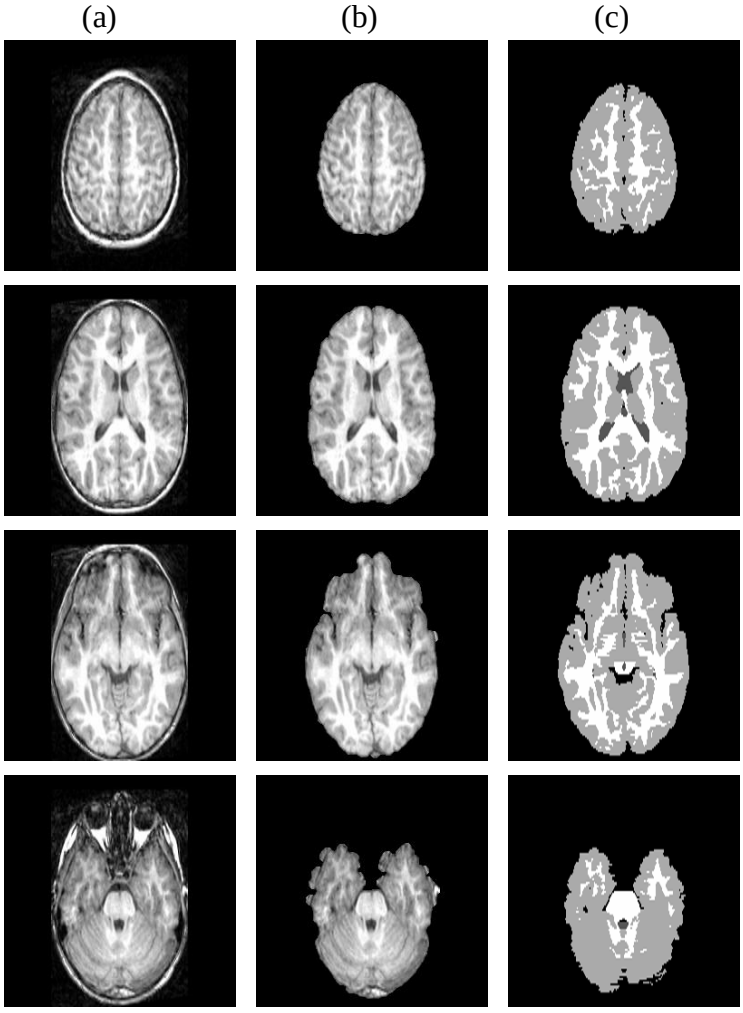

Figure 5.4 Skull stripped IBSR brain MR images. Columns from left to right: a) original brain images b) respective skull stripped images by the proposed method, c) the skull stripped and tissue segmented ground truth provided by IBSR

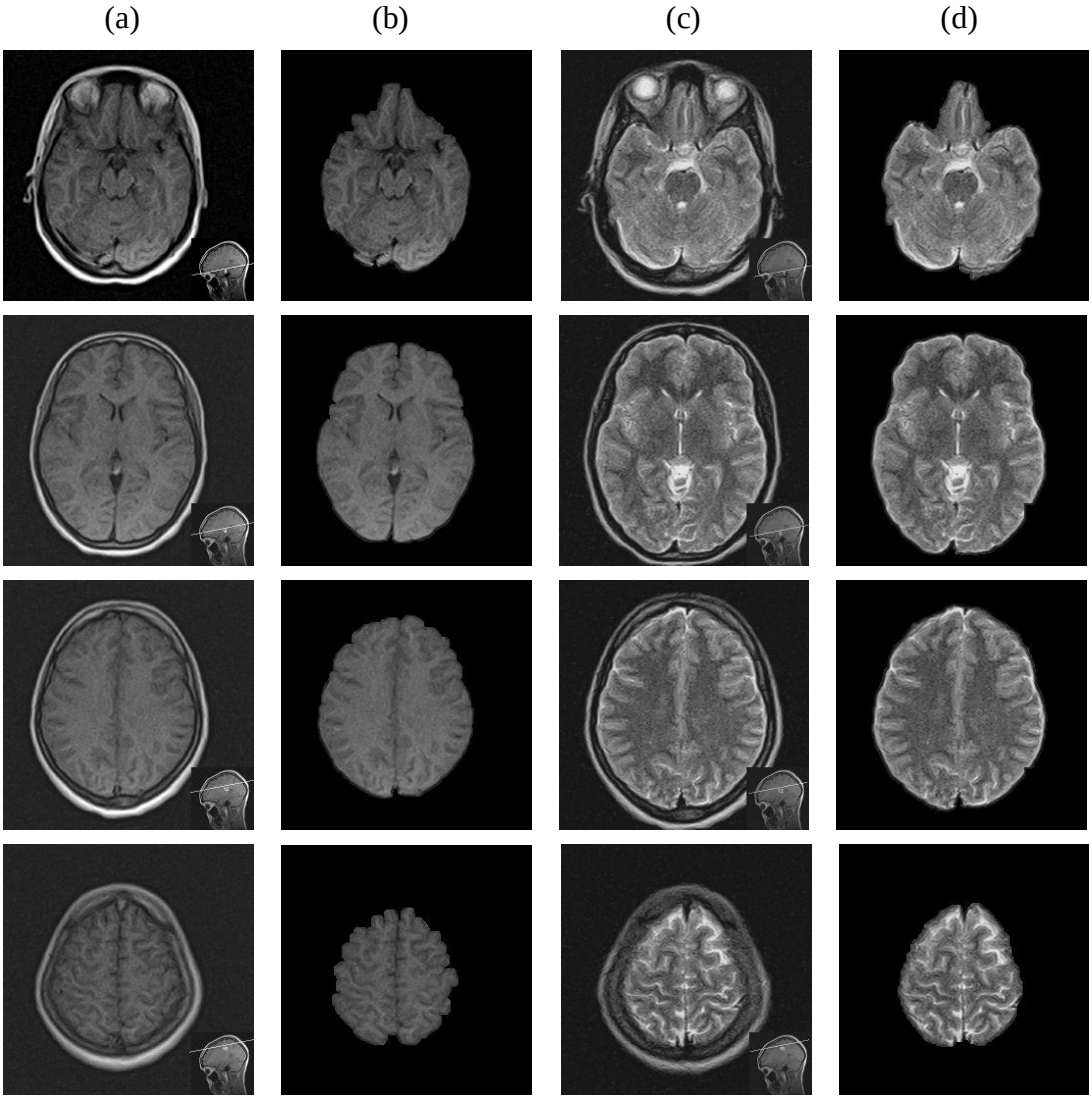

Figure 5.5 Skull stripping on PDC's datasets. Columns from left to right: a) T1-w images b) corresponding skull stripped images c) corresponding T2-w images d) corresponding skull stripping result on T2-w images

In this thesis, skull stripping results attained by implementing the proposed skull stripping technique are at an acceptable level. But, in some instances especially at lower and upper slices where brain tissues are not strongly connected there is relatively small amount of brain tissue loss.

5.5.2 Tumorous Slice Detection Performance Measure

The next module in the proposed framework is tumorous slice detection, in which T1-w and T2-w brain MR images are co-registered, fused and then symmetry analysis is performed on each fused image to detect tumor.

The first task in this second module is to spatially align T1-w (template) image and T2-w (floating) image as described in section 3.3.1. After performing registration in T1-w and T2-w brain MR images, the next step is to fuse the T1-w (template) image with registered T2-w images. Fusion is carried out using the method described in section 3.3.2.

Finally, in this second module we perform symmetry based tumor detection which will enhance the efficiency of the final module of the proposed framework, i.e., tumor segmentation and visualization. The technique used to symmetrically based tumor detection is presented in section 3.3.3 and here we are going to evaluate the efficiency of the method. For tumorous slice detection G_T and O_M are compared based on a value manually set for a brain slice whether it is tumorous or not (1 - tumorous and 0 - non tumorous) and value set by proposed method (1- Jeffrey divergence threshold > 0.0078 and 0 - Jeffrey divergence threshold ≤ 0.0078). Then we evaluate the performance of this tumorous slice detection phase based on the number of slices which are correctly classified as tumorous or non tumorous. Since comparison is performed based on brain slices we use metrics like, how many slices are correctly classified as tumorous slices (T_P), how many slices are wrongly classified as tumorous slices (F_P), how many tumorous slices are wrongly classified as non-tumorous (F_N) and how many non-tumorous brain slices are classified as non-tumorous (T_N). In Table 5.2 true positive ratio (sensitivity) represents the ratio of number of detected true positive (tumorous) slices to ground truth tumorous slices and true negative ratio (specificity) represents ratio of number of detected true negative (non-tumorous) slices to ground truth non-tumorous slices.

Table 5.2 Tumorous slice classification results for PDC dataset.

Cases	**Ground truth**		**Classification of slices by the automatic proposed method**							
	Tumorous	Non-Tumorous	T_P	T_N	F_N	F_P	True positive ratio (Sensitivity)		True negative ratio (Specificity)	
Patient A	5	9	4	4	1	5	(4/5)	0.8000	(4/9)	0.4444
Patient B	7	7	7	7	0	0	(7/7)	1.0000	(7/7)	1.0000
Patient C	10	4	10	4	0	0	(10/10)	1.0000	(4/4)	1.0000
patient D	8	6	7	6	1	0	(7/8)	0.8750	(6/6)	1.0000
Patient E	7	7	6	6	1	1	(6/7)	0.8571	(6/7)	0.8571
Patient F	9	5	8	4	1	1	(8/9)	0.8889	(4/5)	0.8000
Patient G	9	5	9	4	0	1	(9/9)	1.0000	(4/5)	0.8000
Total	55	43	51	35	4	8	(51/55)	0.9273	(35/43)	0.8140

Tables 5.2 and 5.3 show tumorous slice detection results of our method compared against ground truth. The classification of slices into tumorous and non-tumorous is done on total of 728 slices of which 98 slices from 7 patients of PDC dataset and the remaining 630 slices from 9 simulated brain tumor datasets. The result obtained is encouraging at 0.9273 true positive ratio (sensitivity) and 0.8140 true negative ratio (specificity) for PDC datasets as shown on Table 5.2. Also the result obtained for simulated brain tumor dataset is with true positive ratio (sensitivity) of 0.8244 and true negative ratio (specificity) of 0.8267. But, excluding S08 dataset, where symmetry based tumorous slice detection fails, the true positive ratio (sensitivity) reaches 0.9180 and true negative ratio (specificity) becomes 0.8025 as shown on Table 5.3.

As shown on Tables 5.2 and 5.3 the sensitivity and specificity of the classification result varies for different cases in both simulated and real datasets. For example, on PDC's datasets of Patient B, Patient C and Patient G we obtained a maximum sensitivity which equals 1, this means all ground truth tumorous slices were classified as true positives. Among the total number of ground

truth tumorous slices in PDC's dataset only 4 slices are wrongly detected as false negative and among non-tumorous ground truth slices 8 slices are wrongly detected as tumorous slices (false positives). Similarly, for simulated tumor datasets total false positives are 48 slices while false negatives are 26 slices, excluding S08.

Table 5.3 Tumor slice classification for simulated tumor datasets

Cases	**Ground truth slices**		**Classification of slices by the automatic proposed method**							
	Tumorous	Non-Tumorous	T_P	T_N	F_N	F_P	True positive ratio (sensitivity)		True negative ratio (specificity)	
S01	49	21	49	8	0	13	(49/49)	1.0000	(8/21)	0.3810
S02	31	39	31	31	0	8	(31/31)	1.0000	(31/39)	0.7949
S03	30	40	29	40	1	0	(29/30)	0.9667	(40/40)	1.0000
S04	36	34	26	30	10	4	(26/36)	0.7222	(30/34)	0.8824
S05	50	20	41	13	9	7	(41/50)	0.8200	(13/20)	0.6500
S06	22	48	17	48	5	0	(17/22)	0.7727	(48/48)	1.0000
S07	48	22	47	15	1	7	(47/48)	0.9792	(15/22)	0.6818
S08	36	34	0	34	36	0	(0/36)	0.0000	(34/34)	1.0000
S09	51	19	51	10	0	9	(51/51)	1.0000	(10/19)	0.5263
Total	353	277	291	229	62	48	(291/353)	0.8244	(229/277)	0.8267
Total Excluding S08	317	243	291	195	26	48	(291/317)	0.9180	(195/243)	0.8025

The worst sensitivity for the simulated dataset, $S08$, is achieved due to the nature of the tumor, i.e., its approximately bilateral appearance which results in approximately the same probability distribution of intensities on both hemispheres of the brain where symmetry based brain tumor detection fails. But this case is not common in real (clinically acquired) tumorous brain dataset.

Other cases of false negatives are mainly at the beginning and ending of tumors region in slices where the tumor is small in size and isointense to the normal tissues. Similarly, false positives are mainly due to the asymmetric nature of brain MRI slice at the paranasal sinuses (below the eyes) regions.

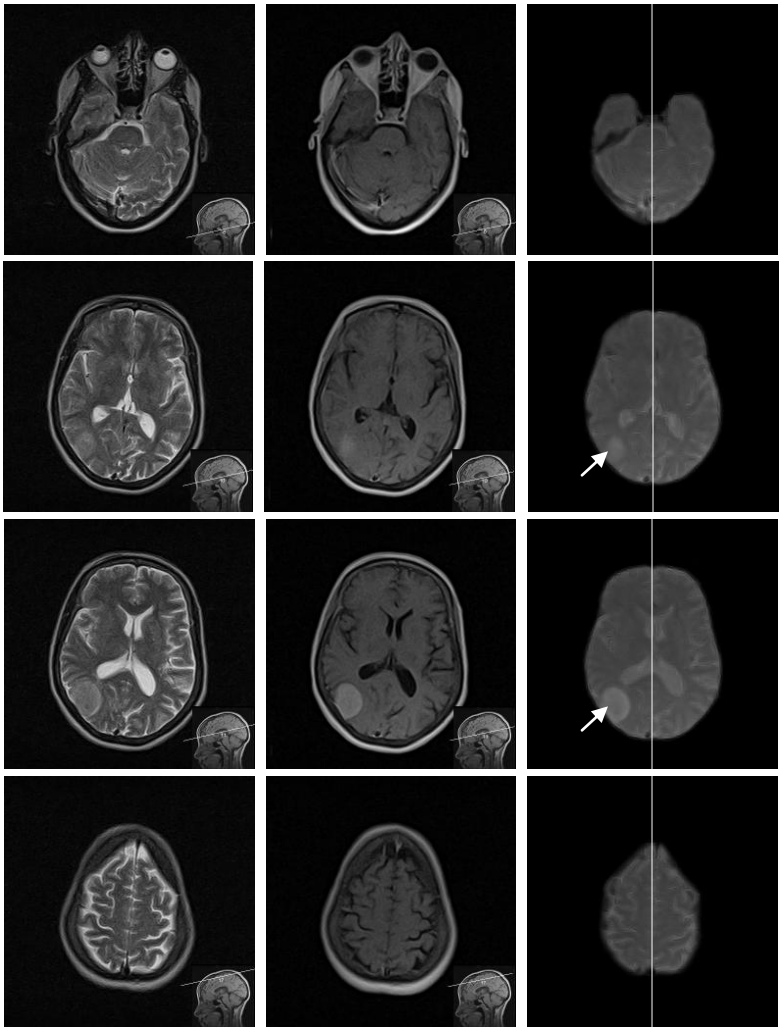

Figure 5.6 Sample result of classification of slices into tumorous or non tumorous for PDC's Patient A. Columns from left to right: T2-w image, T1-w image, and fused and symmetry line extracted image. Rows from top to bottom: false positive, false negative, true positive and true negative. Tumor regions are indicated by arrows.

Sample results of brain tumors that were correctly detected (true positives and true negatives) and incorrectly detected (false positives and false negatives) for the cases of simulated tumor dataset are shown in Figure 5.7.

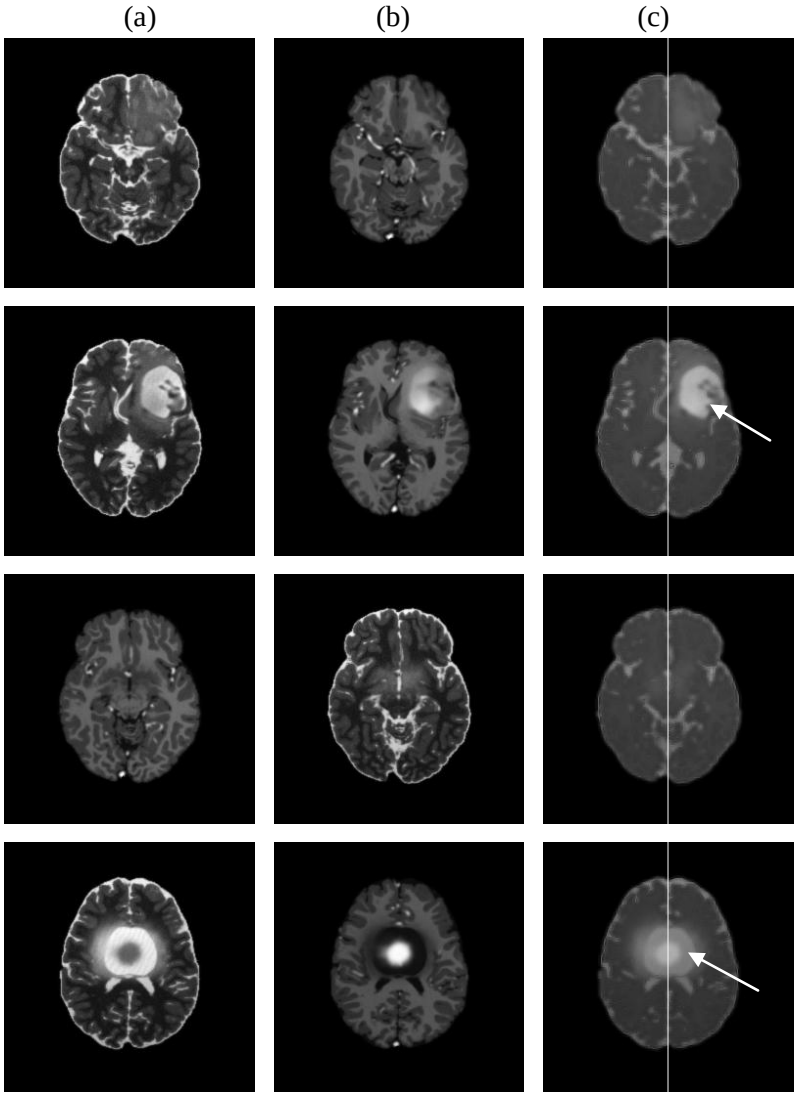

Figure 5.7 Sample results of classification of slices into tumorous or non tumorous for simulated tumor dataset. Columns from left to right: (a) T2-w image, (b) T1-w image and (c) fused and symmetry line extracted image. Rows from top to bottom, row 1 and 2: false positive and true positive cases of S01 respectively. Row 3 and 4: true negative and false negative cases of S08 respectively. Tumor regions are indicated by arrows.

5.5.3 FHNN Tumor Segmentation Performance Measure

Until now, we have seen the results at each subsequent modules of the proposed framework. Here, we evaluate the FHNN based brain tissues and tumor segmentation method that performs tumor segmentation (detection of tumorous region) and visualization processes.

We used the FHNN described in section 4.2.3 to segment tumorous datasets presented in section 5.3. To validate the efficiency of the proposed method on these datasets we used Jaccard similarity measure, Dice similarity score, and sensitivity and specificity metrics. Here, for the segmentation case the metrics are defined based on pixels in the image as follows. Let P be the set of all pixels in the image, $G_T \in P$ be the set of pixels that were labeled as a tumor by ground truth and $O_M \in P$ be the set of pixels that were labeled as tumor by our method. Then the total four possible outcomes are defined as: $T_P = G_T \cap O_M, T_N = \overline{G_T} \cap \overline{O_M}$, $F_P = \overline{G_T} \cap O_M$ and $F_N = G_T \cap \overline{O_M}$ for tumorous pixels in G_T andO_M. The metrics in equations 5.1, 5.2, 5.3 and 5.4 are similarly updated to pixel level.

Quantitative validation of the tumor segmentation method has been performed on 9 simulated brain tumor datasets on total number of 326 slices including S08 datasets where segmented tumor ground truth is provided. We test the performance of the segmentation method on tumorous slices by excluding false positive cases and including false negative cases in the input data for the segmentation stage. Each simulated brain dataset represents different tumor shape, location, size, image intensity and appearance. Table 5.4 shows the quantitative results of the segmentation method using Jaccard similarity index, Dice similarity score, sensitivity and specificity against ground truth. The result obtained is encouraging at mean Jaccard similarity index of maximum of 0.9353, minimum of 0.8016 and average of 0.8569 among datasets. The obtained mean of Dice similarity score includes maximum of 0.9665, minimum of 0.8876 and average of 0.9186. Also mean of sensitivity varies from 0.9114 to 0.9850 with average of 0.9480 and mean of specificity varies from 0.9717 to 0.9996 with average of 0.9917.

Jaccard similarity index and Dice similarity score evaluate the amount of overlap of the extracted tumor region between the proposed method and ground truth.

Table 5.4 *Mean (standard deviation)* value of Jaccard similarity index (JSI), Dice similarity score (DSS), sensitivity and specificity for tumor segmentation

Data	JSI	DSS	Sensitivity	Specificity
S01	0.9048 (0.0362)	0.9497 (0.0202)	0.9206 (0.0389)	0.9996 (0.0001)
S02	0.8562 (0.1524)	0.9138 (0.1110)	0.9842 (0.0173)	0.9976 (0.0034)
S03	0.8482 (0.1079)	0.9143 (0.0639)	0.9791 (0.0313)	0.9977 (0.0023)
S04	0.8784 (0.1458)	0.9245 (0.1440)	0.9360 (0.0435)	0.9717 (0.1642)
S05	0.9353 (0.0123)	0.9665 (0.0064)	0.9372 (0.0162)	0.9730 (0.1644)
S06	0.8061 (0.0967)	0.8894 (0.0639)	0.9850 (0.0173)	0.9984 (0.0012)
S07	0.8539 (0.0827)	0.9191 (0.0497)	0.9385 (0.0777)	0.9967 (0.0039)
S08	0.8016 (0.0795)	0.8876 (0.0526)	0.9396 (0.0526)	0.9938 (0.0052)
S09	0.8274 (0.0928)	0.9024 (0.0629)	0.9114 (0.0666)	0.9971 (0.0037)
Average	0.8569 (0.0896)	0.9186 (0.0638)	0.9480 (0.0402)	0.9917 (0.0387)

While sensitivity measures the ratio of accurately identified tumor pixels (true positives) by the system to the ground truth actual tumor pixels and specificity measures the ratio of accurately identified non-tumor pixels (true negatives) by the system to the ground truth actual non-tumor pixels. Based on these quantitative evaluations the result on Table 5.4 shows a good accuracy of the segmentation method. Qualitatively Figure 5.8, Figure 5.9 and Figure 5.10 show sample segmentation results on simulated tumor and PDC datasets. Sample results on non-tumorous tissue segmentation are given in Figure 5.11. The qualitative results show the effectiveness of the proposed method in segmenting brain tumors and normal brain tissues in brain MR images, though it has some difficulties in segmenting brain tissues in low tissue contrast MR images, for instance the case of PDC dataset.

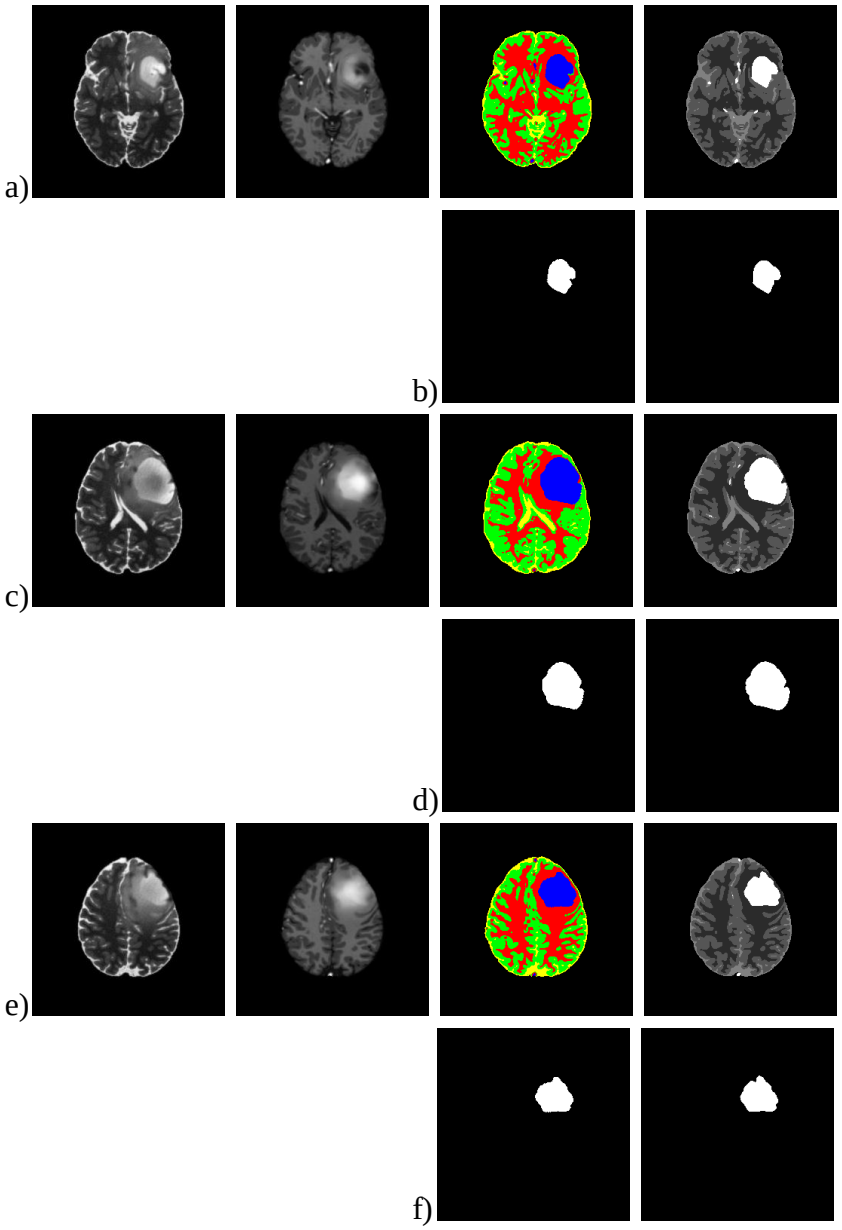

Figure 5.8 Sample results of tumor segmentation and extraction on S01 simulated tumor dataset. Rows (a), (c) and (e): columns from left to right: T2-w image, T1-w image, segmented image by the system and ground truth segmented tumor. Rows (b), (d) and (f): columns from left to right: extracted tumor by the proposed method and extracted ground truth tumor region

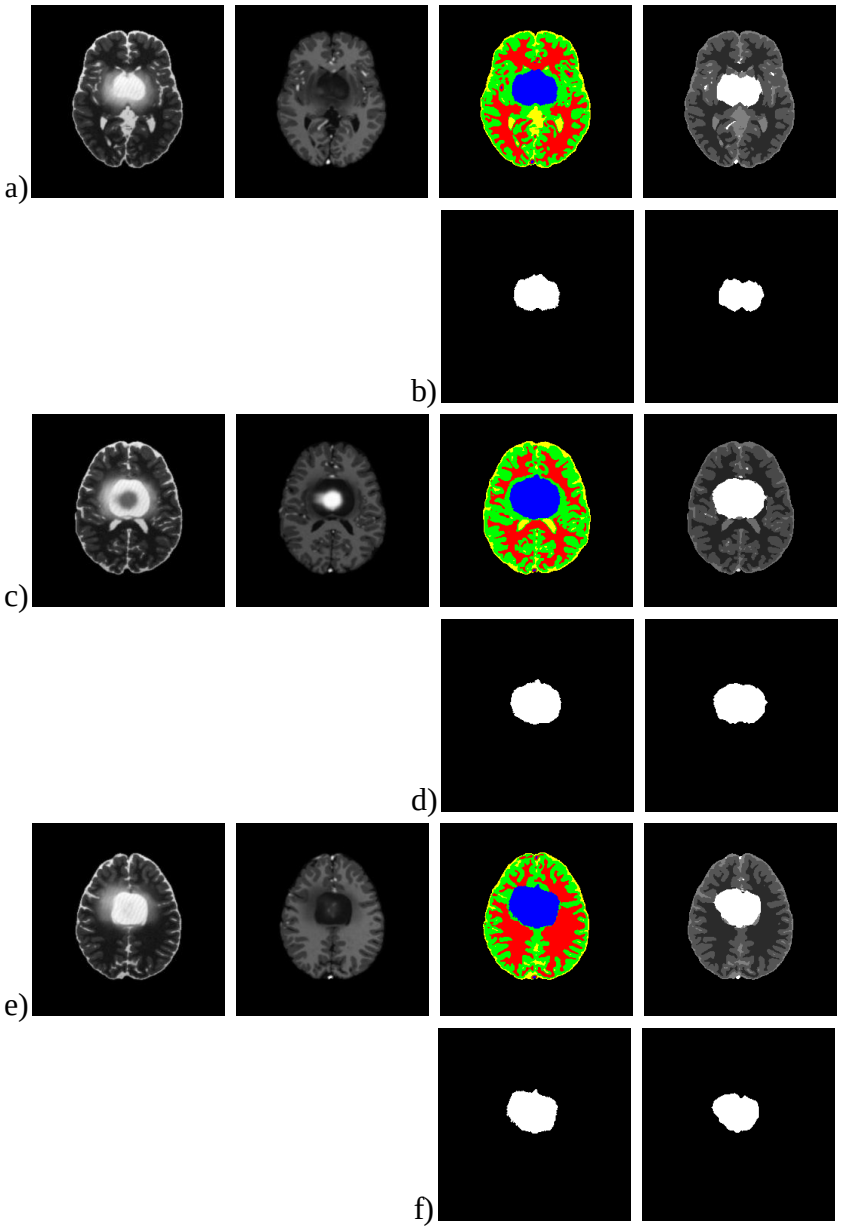

Figure 5.9 Sample results of tumor segmentation and extraction on middle brain tumor, S08 simulated tumor dataset. Rows (a), (c) and (e): columns from left to right: T2-w image, T1-w image, segmented image by the system and ground truth segmented tumor. Rows (b), (d) and (f): columns from left to right: extracted tumor by the proposed method and extracted ground truth tumor region

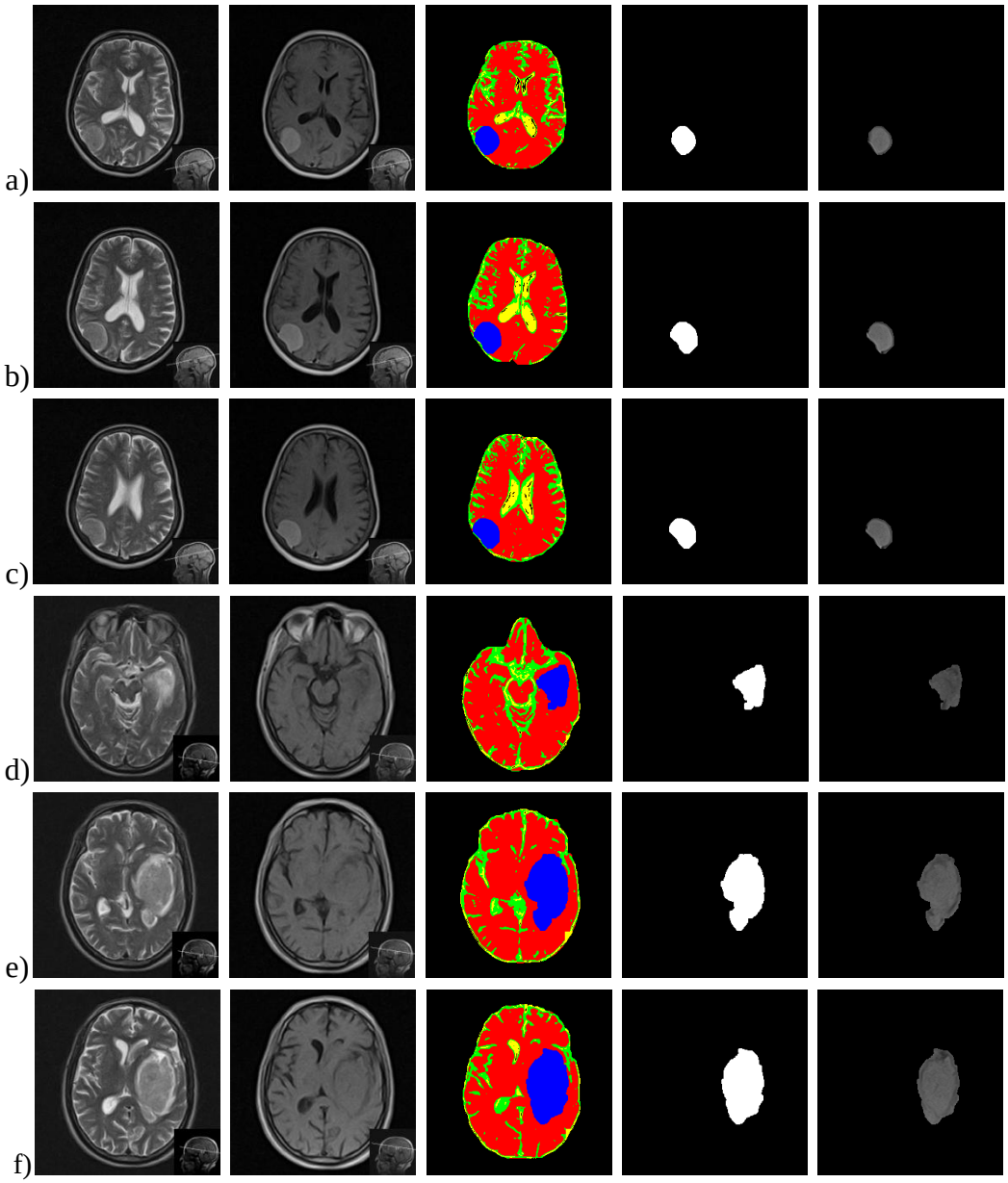

Figure 5.10 Sample results of tumor segmentation and extraction on PDC datasets. Rows (a), (b) and (c): columns from left to right: Patient A's T2-w image, T1-w image, segmented image by the system, extracted tumor from segmented image and extracted tumor region from T1-w image. Rows (d), (e) and (f): columns from left to right: Patient B's T2-w image, T1-w image, segmented image by the system, extracted tumor from segmented image and extracted tumor region from T1-w image.

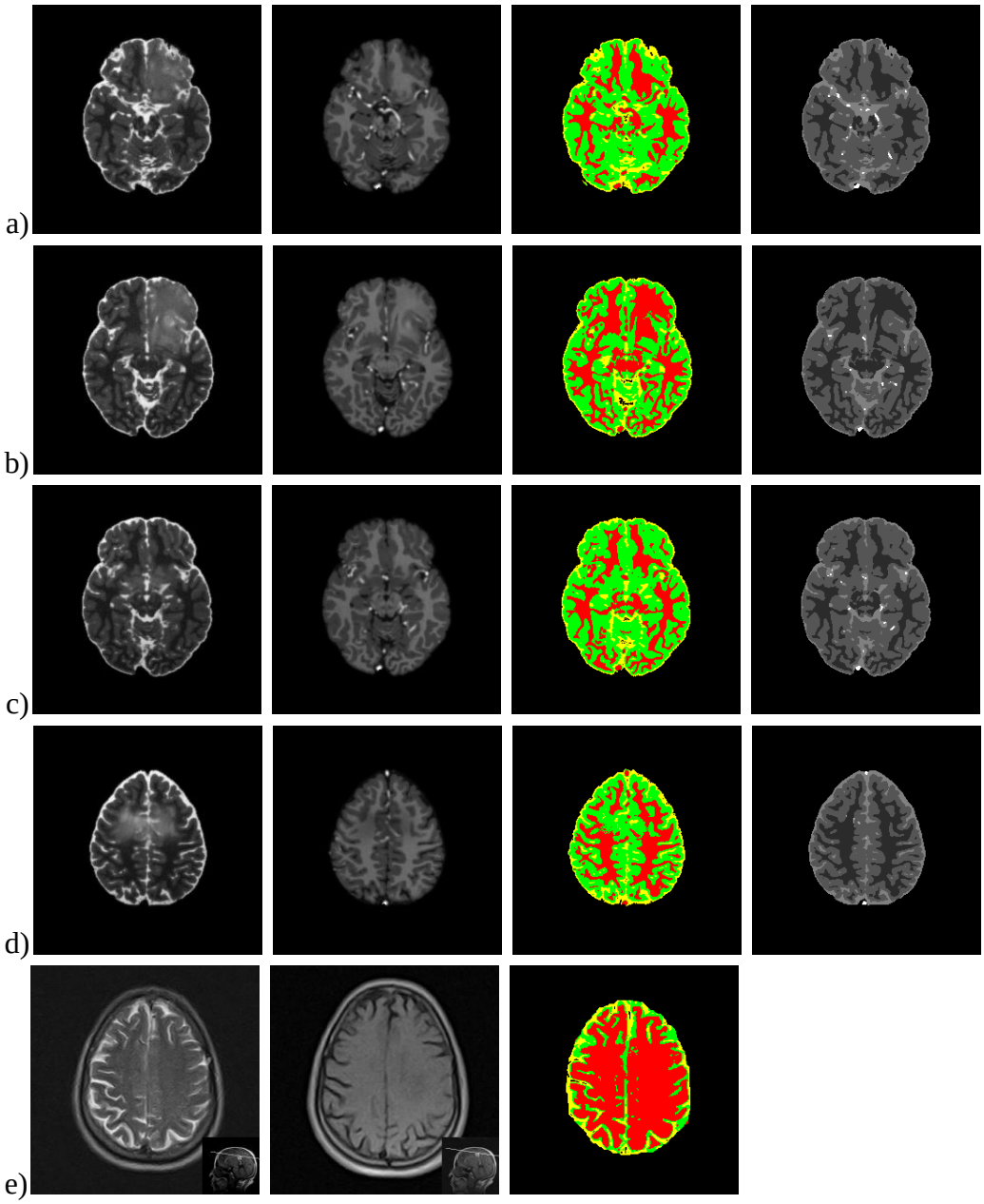

Figure 5.11 Sample result of non-tumorous slices brain tissue segmentation. Rows (a), (b) and (c) and (d): columns from left to right: From simulated tumor datasets T2-w image, T1-w image, segmented image by the proposed system and ground truth tissue segmentation. Row (e): columns from left to right: From PDC datasets T2-w image, T1-w image and segmented image by the proposed system.

Regarding to the computation time, on average the system takes 1.5 minutes to detect and segment each MRI brain slice on Intel core $i3$ 2.27 GHz laptop of 2 GB RAM. From this total time preprocessing, i.e., skull stripping and inhomogeneity correction on average takes 1.3 seconds. The second module, tumorous slice detection, on average takes 31 seconds in image registration, 17 seconds in image fusion and 33 seconds in symmetry analysis. The third module tumor segmentation and visualization on average takes 1.04 seconds in initial tumor segmentation by FHNN using fused image and 0.84 seconds in tumor segmentation refinement using tumor superimposed T1-weighted image. This indicates the computational efficiency of the fuzzy Hopfield neural network in segmenting brain tumors in MR images in less than 2 seconds even though the second module takes relatively longer time.

Chapter 6

Conclusion and Recommendation for Future Works

6.1 Conclusions

In this thesis research, a step by step methodology for automatic and unsupervised brain tumor segmentation using fuzzy Hopfield neural network is presented. To realize an automatic and unsupervised segmentation we implement a framework that utilizes a combination of different techniques and composed of three modules. The first module used to remove non-brain tissues (skull stripping) and to reduce noise and intensity inhomogeneity from brain MR images. The second module implements image registration, fusion and symmetry analysis. In this stage fusion of T1-weighted and T2-weighted images and detection of tumorous slice is performed, which facilitates the final segmentation of normal tissues and tumor region from brain MR images in the third module using fuzzy Hopfield neural network.

The principal advantages of the proposed framework are, first it does not need training data. Second it is capable to segment normal tissues and both enhanced and non-enhanced tumors by fusing T1-weighted and T2-weighted images. Thirdly, it can be implemented as real time application due to high speed segmentation ability of fuzzy Hopfield neural network. Finally, the proposed framework is highly automatic in that little or no user intervention is required to produce normal tissues and tumor segmentation results in a limited time.

The performance of the proposed framework is evaluated on various MR images including simulated and real, normal and tumorous. Quantitatively the method is validated against ground truth using commonly used validation metrics, i.e., Jaccard similarity index, Dice similarity score, sensitivity and specificity. Even though there is no common standard (implementation and datasets) to compare our method against with existing methods, the quantitative results of our proposed framework are comparable to the most recent works reported in literature [14, 19, 32, 33, 34, 43].

6.2 Recommendations to Future Works

The tumor detection and segmentation result obtained by the proposed framework is evaluated by experienced radiologist at Pioneer Diagnostic Center. According to the radiologist the result of our proposed framework is promising. In the future, the work of this thesis research can be extended to increase the detection and segmentation accuracy. Here are list of recommendations to possible extensions of the works of this thesis research:

- The implemented system is tested on stack 2-D brain MRI axial slices and no correlation between slices is performed. However, if it is extended by performing correlation between, the detection and segmentation accuracy may be improved. Also 3-D visualization of tumor region becomes possible.
- The skull stripping technique implemented in this thesis research assumes brain is the largest connected region in the brain MRI scans. But, in some instances especially at lower and upper slices where brain tissues are not strongly connected there is relatively small amount of brain tissue loss. So, to fully automate the proposed system this drawback has to be solved.
- Image registration and fusion takes relatively longer time compared to time required for tumor segmentation in fuzzy Hopfield neural network, enhancing these stages will enable us to fully exploit the computationally efficiency of FHNN.
- Approximately bilateral appearance of brain tumors in MR images which results in approximately the same probability distribution of intensities on both hemispheres of the brain may not be detected by symmetry based brain tumor detection. Even though this case is not common in real (clinically acquired) tumorous brain dataset, it is required to detect this kind of cases to fully automate the classification of tumorous slices from non-tumorous one.

References

[1] Jan C. Buckner, et al., "Central Nervous System Tumors", *Mayo Clinic Proceedings*, Vol. 82, No. 10, 2007, pp. 1271-1286.

[2] Charles R. Noback, Norman L. Strominger, Robert J. Demarest and David A. Ruggiero, *The Human Nervous System: Structure and Function*, 6th ed., Humana Press, 2005.

[3] Ferlay J, Shin HR, Bray F, Forman D, Mathers C and Parkin DM, "GLOBOCAN 2008 v2.0, Cancer Incidence and Mortality Worldwide", *International Agency for Research on Cancer, Lyon, France*, 2010. *http://globocan.iarc.fr*, Accessed on: November 13, 2011.

[4] Youcef Chibani and Amrane Houacine, "Redundant Versus orthogonal wavelet Decomposition for multisensory image fusion", *Pattern Recognition (Elsevier)*, Vol. 36, Issue 4, April 2003, pp. 879-887.

[5] Schmidt M. , Levner I. , Greiner R. , Murtha A. and Bistritz A., "Segmenting Brain Tumors using Alignment-Based Features", *IEEE 4th International Conference on Machine Learning and Applications, ICMLA*, Dec. 2005, pp. 215-220.

[6] *http://www.radiologyassistant.nl/*, Accessed on: January,12,2012

[7] Louis D.N., Ohgaki H., Wiestler O.D, Cavenee W.K. (Eds.), "WHO Classification of Tumors of the Central Nervous System", *International Agency for Research on Cancer (IARC), Lyon, France*, 2007.

[8] Hsieh et al., "Automatic Segmentation of Meningioma From Non-contrasted Brain MRI Integrating Fuzzy clustering and Region Growing", *BMC Medical Informatics and Decision Making*, 11:54, Published online 2011 August 26. doi: 10.1186/1472-6947-11-54.

[9] Sezgin M. and Sankur B.,"Survey over image thresholding techniques and quantitative performance evaluation", *Journal of Electronic Imaging* ,Vol. 13,No. 1 , Jan. 2004, pp. 146–165.

[10] Stavri Nikolov, Paul Hill, David Bull, and Nishan Canagarajah,"Wavelets for Image Fusion," *Wavelets in Signal and Image Analysis, Computational Imaging and Vision Series*, Kluwer Academic Publishers, Dodrecht, the Netherlands, 2001, pp. 213–244.

[11] Farhad Mohamad, et al, "Fast Image Segmentation Using C-Means Based Fuzzy Hopfield Neural Network", *IEEE, Canadian Conference on Electrical and Computer Engineering*, May 3008, pp. 1855-1860.

[12] Hua-mei Chen and Pramod K. Varshney, "Mutual Information-Based CT-MR Brain Image Registration Using Generalized Partial Volume Joint Histogram Estimation", *IEEE Transactions on Medical Imaging*, Vol. 22, No.9, Sep. 2003, pp. 1111-1119.

[13] S.Xavierarockiaraj, K.Nithya, and R.Maruni Devi, "Brain Tumor Detection Using Modified Histogram Thresholding-Quadrant Approach", *Journal of Computer Applications (JCA)*, Vol. 5, No.1, 2012, pp. 21-25.

[14] Zhang et al, "An Automated and simple method for brain MR image extraction", *Biomedical Engineering online*, 2011, 10:81, Published online 2011 September 13. doi: 10.1186/1475-925X-10-81.

[15] Sadananthan et al., "Skull stripping using graph cuts", *NeuroImage*, Vol. 49, Issue 22 , January 2010, pp. 225-239.

[16] Kadam D. B., Gade S. S., M. D. Uplaneand R. K. Prasad, "Neural Network Based Brain Tumor Detection Using MR Images", *International Journal of Computer Science and Communication (IJCSC)*, Vol. 2, No.2, July-Dec. 2011, pp. 325-331.

[17] Anam Mustaqeem, Ali Javed and Tehseen Fatima, "An Efficient Brain Tumor Detection Algorithm Using Watershed and Thresholding Based Segmentation", *International Journal of Image, Graphics and Signal Processing (IJIGSP)*, Vol. 4, No.10, 2012, pp. 34-39.

[18] Kai Xie , Jie Yang , Z.G. Zhang and Y.M. Zhu, "Semi-automated brain tumor and edema segmentation using MRI", *European Journal of Radiology*, Vol. 56 , Issue 1, October 2005, pp. 12 -19.

[19] Hassan Khotanlou, Olivier Colliot, Jamal Atif and Isabelle Bloch, "3D brain tumor segmentation in MRI using fuzzy classification, symmetry analysis and spatially constrained deformable models", *Fuzzy Sets and Systems*, Vol. 160, Issue 10, 2009, pp.1457–1473.

[20] Rafael C. Gnzalez and Richard E. Woods, *Digital Image Processing*, Prentice Hall, New Jersey,2nd ed., 2002, pp. 519-567

[21] Pohle R, Toennies KD; "Segmentation of medical images using adaptive region growing", *Proceedings of SPIE-Medical Imaging*, Vol. 4322, 2001, pp. 1337-1346.

[22] Nikola K. Kasabov, *Foundations of Neural Networks, Fuzzy Systems, and Knowledge Engineering*, Massachusetts Institute of Technology, 1998, pp. 167-473

[23] M. Egmont-Petersen, D. de Ridder and H. Handels, "Image processing with neural networks—a review", *Pattern Recognition*, Vol. 35, Issue 10, Oct. 2002, pp. 2279-2301.

[24] Uros Vovk, Franjo Pernus and Bostjan Likar, "A Review of Methods for Correction of Intensity Inhomogeneity in MRI", *IEEE Transaction in Medical Imaging*, Vol. 26, No. 3, March 2007, pp. 405-421.

[25] Olivier Salvado, Claudia Hillenbrand, Shaoxiang Zhang and David L. Wilson, "Method to Correct Intensity Inhomogeneity in MR Images for Atherosclerosis Characterization", *IEEE Transactions on Medical Imaging*, Vol. 25, No.5, May 2006, pp. 539- 552.

[26] Mehmed Ozkan, Benoit M. Dawant and Robert J. Maciunas, "Neural Network Based Segmentation of Multi-Modal Medical Images: A comparative and Prospective Study", *IEEE Transaction on Medical Imaging*, Vol. 12, No. 13, Sept. 1993, pp. 534-544.

[27] T. Logeswari and M. Karnan, "An improved implementation of brain tumor detection using segmentation based on soft computing", *Journal of Cancer Research and Experimental Oncology*, Vol. 2, No. 1, March 2010, pp. 006-014.

[28] F. Se´gonne et al, "A hybrid approach to the skull stripping problem in MRI", *NeuroImage*, Vol. 22, Issue 3, July 2004, pp. 1060-1075.

[29] L. J. Erasmus, D. Hurter, M. Naude, H.G. Kritzinger and S Acho, "A short overview of MRI artifacts", *SA Journal of Radiology*, Vol. 8 ,No. 2 , August 2004, pp. 13-17.

[30] L. R. Dice, "Measures of the Amount of Ecological Association between Species", *Ecology*, Vol. 26, No. 3, July 1945, pp. 297-302.

[31] Kuo-Sheng Cheng, Jzau-Sheng Lin and Chi-Wu Mao, "The Application of Competitive Hopfield Neural Network to Medical Image Segmentation", *IEEE Transactions on Medical Imaging*, Vol.15, No. 4, August 1996, pp. 560-567.

[32] Michael Wels, et al., "A Discriminative Model-Constrained Graph Cuts Approach to Fully Automated Pediatric Brain Tumor Segmentation in 3-D MRI", *Lecture Notes in Computer Science, Medical Image Computing and Computer-Assisted Intervention – MICCAI 2008* , Vol. 5241 , 2008 , pp. 67-75.

[33] A. Rajendran and R.Dhanasekaran, " A hybrid Method Based on Fuzzy Clustering and Active Contour Using GGVF for Brain Tumor Segmentation on MRI Images", *European Journal of Scientific Research*, Vol. 61, No. 2, 2011, pp. 305-313.

[34] Gordillo, N., Montseny, E., Sobrevilla, P. ,"A New Fuzzy Approach to Brain Tumor Segmentation", *Fuzzy Systems (FUZZ), 2010 IEEE International Conference on* , 18-23 July 2010, pp.1-8, , doi: 10.1109/FUZZY.2010.5584178

[35] J. C. Dunn, "A Fuzzy Relative of the ISODATA Process and Its Use in Detecting Compact Well-Separated Clusters", *Journal of Cybernetics*, Vol. 3, No.3, 1973, pp. 32-57.

[36] James C. Bezdek, Robert Ehrlich and William Full, "FCM: The Fuzzy C-Means Clustering Algorithm", *Computer and Geosciences*, Vol. 10, No. 2-3, 1984, pp. 193-203.

[37] M. Arfan Jaffar,Quratulain,and Tae Sun Choi, "Tumor Detection From Enhanced Magnetic Resonance Imaging Using Fuzzy Curvelet", *Microscopy Research and Technique, Wiley Online Library*, Vol. 75, No. 6, April 2012, pp. 499- 504.

[38] James E. Fowler, "The Redundant Discrete Wavelet Transform and Additive Noise", *IEEE signal Processing Letters*, Vol. 12, Sep. 2005, pp. 629-632.

[39] Nobuyuki Otsu, " A threshold Selection Method from Gray-Level Histograms", *IEEE Transactions on Systems, Man, and Cybernetics*, Vol. 9, No.1, January 1979, pp. 62-66.

[40] Yong Yang, Dong Sun Park, Shuying Huang and Nini Rao, "Medical Image Fusion via an Effective Wavelet- Based Approach", *EURASIP Journal on Advances in Signal Processing*, Article ID 579341, 2010, pp. 1-13.

[41] Xuesong Lu, Su Zhang, He Su and Yazhu Chen, "Mutual information-based multimodal image registration using a novel joint histogram estimation", *Computerized Medical Imaging and Graphics*, Vol. 32, Issue 3 , April 2008, pp. 202-209.

[42] Humayun Karim Sulehria and Ye Zhang, "Hopfield Neural Networks- A Survey", *Proceedings of the 6th WSEAS Int. Conf. on Artificial Intelligence, Knowledge Engineering and Data Bases*, Corfu Island, Greece, February 16-19, 2007, pp.125 -130.

[43] Kishore K. Reddy, et al, " Confidence Guided Enhancing Brain Tumor Segmentation in Multi-Parametric MRI", *9th IEEE International Symposium on Biomedical Imaging*, May 2012, pp. 366-369.

[44] J. Zhou, K. L. Chan, V. F. H. Chong and S. M. Krishnan, "Extraction of Brain Tumor from MR Images Using One-Class Support Vector Machine", *Proceedings of the 2005 IEEE: Engineering in Medicine and Biology 27th annual conference*, Shanghai- China, 1-4 Sep. 2005, pp. 6411- 6414.

[45] Indah Soesanti, Adhi Susanto, Thomas Sri Widodo and Maesadji Tjokronagoro, "MRI Brain Images Segmentation Based on Optimized Fuzzy Logic and Spatial Information", *International Journal of Video and Image Processing and Network Security*, Vol. 11, No. 04, August 2011, pp. 6-11.

[46] Nandita Pradhan and A.K. Sinha, "Fuzzy ANN Based Detection and Analysis of Pathological and Healthy Tissues in FLAIR Magnetic Resonance Images of Brain", *international Journal of Information Technology and Knowledge Management*, Vol. 4, No. 2, July-Dec. 2011, pp. 471-476.

[47] Noor Elaiza Abdul Khalid, Shafaf Ibrahim and Mazani Manaf, "Brain Abnormalities Segmentation Performances Contrasting: Adaptive Network-Based Fuzzy Inference System (ANFIS) vs K-Nearest Neighbors (k-NN) vs Fuzzy c-Means (FCM)", *15th WSEAS International Conference on Computers*, Corfu Island, Greece, July 2011, pp. 285-290.

[48] Nahla Ibraheem Jabbar and Monica Mehrotra, "Application of Fuzzy Neural Network for Image Tumor Description", *World Academy of Science, Engineering and Technology*, Issue. 20, August 2008, pp. 575-577.

[49] Jzau-Sheng Lin, Kuo-Sheng Cheng and Chi-Wu Mao, "A Fuzzy Hopfield Neural Network for Medical Image Segmentation", *IEEE Transactions on Nuclear Science*, Vol. 43, No. 4, August 1996, pp. 2389-2398

[50] Midas at Kitware, Open Source Server, Longitude with Pathology Challenge, Simulated Magnetic Resonance Imaging Brain Tumors, *http://midas3.kitware.com/midas/*, accessed on: February 5, 2012

[51] Center for Morphometric Analysis, Massachusetts General Hospital, the Internet Brain Segmentation Repository (IBSR), *http://www.cma.mgh.harvard.edu/ibsr/*, accessed on: November 10, 2011.

[52] Richa Singh, Mayank Vatsa and Alfzel Noore, "Multimodal Medical Image Fusion Using Redundant Discrete wavelet Transform", *Proceedings of the 2009 IEEE 7th International Conference on Advances in Pattern Recognition*, February 04-06,2009, pp. 232-235.

[53] Steven S. Coughlin and Linda W. Pickle, "Sensitivity and Specificity-Like Measures of the Validity of a Diagnostic Test That are Corrected for Chance Agreement", *Epidemiology*, Vol. 3, No. 2, March 1992, pp. 178-181.

[54] Laboratory of Neuroinformatics, Weill Medical College of Cornell University, *http://www.ia.unc.edu/dev/download/imconvert/*, accessed on: February 5,2012

[55] Barbara Zitova and Jan Flusser, "Image registration methods: a survey", *Image and Vision Computing*, Vol. 21, Issue 11, 2003, pp. 977-1000.

[56] J.J. Hopfield, " Neural Networks and Physical Systems with Emergent Collective Computational Abilities", *Proceedings of the National Academy of Sciences of the United States of America*, vol. 79, April 1982, pp. 2554-2558

[57] Hang-Da Cheng and Ying Sun, "A Hierarchical Approach to Color Image Segmentation Using Homogeneity", *IEEE Transactions on Image Processing*, Vol. 9, No. 12, Dec. 2000, pp. 2071-2082.

[58] Paul Jaccard, "The Distribution of the Flora in the Alpine Zone", *The New Phytologist*, Vol. 11, No. 2, February 1912, pp. 37-50.

[59] J.P.W. Pluim, J.B.A. Maintz and M.A. Viergever,"Mutual information matching in multiresolution contexts", *Image and Vision Computing*, Vol. 19, Issue. 1-2, January 2001, pp.45-52.

[60] John Ashburner and Karl J. Friston, "Rigid Body Registration", *Human Brain Function*. Academic Press, 2nd ed., 2003.

[61] Anjali Malviya and S.G Bhirud, " Image Fusion of Digital Images", *International Journal of Recent Trends in Engineering*, Vol. 2, No. 3, Nov. 2009, pp. 146-148.

[62] Yanxi Liu, Robert T. Collins and William E. Rothfus, "Automatic Extraction of the Central Symmetry (Mid-Sagittal) Plane from Neuroradiology Images", *Carnegie Mellon University, The Robotics Institute Technical Report, CMU-RI-TR-96-40,* December, 1996

[63] Alexander V. Tuzikov, Olivier Colliot and Isabelle Bloch, "Evaluation of the symmetry plane in 3D MR brain Images", *Pattern Recognition Letters*, Vol. 24, Issue 14, October 2003, pp. 2219-2233.

[64] J.-P. Thirion, S. Prima, G. Subsol and N.Roberts, "Statistical analysis of normal and abnormal dissymmetry in volumetric medical images", *Medical Image Analysis*, Vol. 4, Issue 2, June 2000, pp. 111-121.

[65] Nilanjan Ray, Russell Greiner and Albert Mertha, "Using Symmetry to Detect Abnormalities in Brain MRI", *Computer Society of India Communication*, Vol. 31, No. 19, January 2008, pp. 7-10

[66] Peter lorenzen, Sarang Joshi, Guido Geric and Elizabeth Bullitt,"Tumor-Induced Structural and Radiometric Asymmetry in Brain MR Images" *In Proceedings of the IEEE Workshop on Mathematical Methods in Biomedical Image Analysis (MMBIA '01). IEEE Computer Society, Washington, DC, USA*, 2001, pp.163-170.

[67] Sylvain Prima, Jean-Philippe Thirion, Gerard Subsol and Neil Roberts "Automatic analysis of Normal Brain Dissymmetry of Males and Females in MR Images", *Lecture Notes in Computer Science, Medical Image Computing and Computer Assisted Intervention (MICCAI)* , Vol. 1496, 1998, pp.770-779.

[68] Phillips, W.E. et al., " Application of fuzzy c-means segmentation techniques for tissue differentiation in MR images of hemorrhagic glioblastoma multiform", *Magnetic Resonance Imaging*, Vol. 13, Issue 2, 1995, pp. 277-290.

[69] *http://www.teamrads.com/Cases/Neuroanatomy/MRI,* Accessed on: January,12,2012

[70] "Medical Imaging in Cancer Care: Charting The Progress", *US Oncology and National Electrical Manufacturers Association (NEMA),* Accessed on January 20, 2012 at *http://www.healthcare.philips.com/pwc_hc/us_en/about/Reimbursement/assets/docs/cancer_white_paper.pdf*

[71] A. O Rodriguez, " Principles of Magnetic Resonance Imaging", *Revista Mexicana de Fisica*, Vol. 50, No. 3, 2004, pp. 272-286.

[72] Joseph P. Hornark, "The Basics of MRI", Accessed on: January 12, 2012, at http*://www.cis.rit.edu/htbooks/mri/*

[73] Catherine Westbrook, *MRI at Glance*, Blackwell Science Publishing, 2002

[74] Tom M. Mitchell, *Machine Learning*, McGraw-Hill, 1997

[75] Richard O. Duda, Peter E. Hart and David G. Sork, *Pattern Classification, 2nd ed.*, Wiley-Interscince, 1995.

[76] Parastawa M, Bullitt E, Gerig G, "Simulation of Brain Tumors in MRI images for Evaluation of Segmentation Efficacy." *Medical Image Analysis,* Vol. 13, No. 2, April 2009, pp. 297-311.

[77] Niethammer M, Hart G, Pace D, Vespa P, Irimia A, Van Horn J, Aylward S, " Geometric Metamorphosis." *Lecture Notes in Computer Science, Medical Image Computing and Computer Assisted Intervention (MICCAI)* , Vol. 6893, 2011, pp.639-646.